

Fire-Generated Tornadic Vortices

Neil P. Lareau, Nicholas J. Nauslar, Evan Bentley, Matthew Roberts, Samuel Emmerson, Brian Brong, Matthew Mehle, and James Wallman

ABSTRACT: Fire-generated tornadic vortices (FGTVs) linked to deep pyroconvection, including pyrocumulonimbi (pyroCbs), are a potentially deadly, yet poorly understood, wildfire hazard. In this study we use radar and satellite observations to examine three FGTV cases during high-impact wildfires during the 2020 fire season in California. We establish that these FGTVs each exhibit tornado-strength anticyclonic rotation, with rotational velocity as strong as 30 m s⁻¹ (60 kt), vortex depths of up to 4.9 km AGL, and pyroCb plume tops as high as 16 km MSL. These data suggest similarities to EF2+strength tornadoes. Volumetric renderings of vortex and plume morphology reveal two types of vortices: *embedded vortices* anchored to the fire and residing within high-reflectivity convective columns and *shedding vortices* that detach from the fire and move downstream. Time-averaged radar data further show that each case exhibits fire-generated mesoscale flow perturbations characterized by flow splitting around the fire's updraft and pronounced flow reversal in the updraft's lee. All the FGTVs occur during deep pyroconvection, including pyroCb, suggesting an important role of both fire and cloud processes. The commonalities in plume and vortex morphology provide the basis for a conceptual model describing when, where, and why these FGTVs form.

KEYWORDS: Convection; Tornadogenesis; Tornadoes; Wildfires

https://doi.org/10.1175/BAMS-D-21-0199.1

Corresponding author: Neil P. Lareau, nlareau@unr.edu

Supplemental material: https://doi.org/10.1175/BAMS-D-21-0199.2

In final form 22 November 2021 ©2022 American Meteorological Society

For information regarding reuse of this content and general copyright information, consult the AMS Copyright Policy.

AFFILIATIONS: Lareau and Roberts—University of Nevada–Reno, Reno, Nevada; Nauslar—National Interagency Fire Center, Bureau of Land Management, Boise, Idaho; Bentley—Storm Prediction Center, National Weather Service, Norman, Oklahoma; Emmerson—University of Oklahoma, Norman, Oklahoma; Brong—National Weather Service, Reno, Nevada; Mehle—National Weather Service, Monterey, California; Wallman—National Interagency Fire Center, United States Forest Service, Boise, Idaho

ildfires have emerged as a leading societal threat yet are less understood and more difficult to predict than other weather-based disasters (Peace et al. 2020). One key complexity in wildfires is the development of fire-generated severe convective storms (i.e., pyrocumulonimbus, "pyroCb," Fromm et al. 2006, 2010; Terrasson et al. 2019), which can contain extreme updrafts [60 m s⁻¹, 130 mi h⁻¹ (hereinafter mph); Rodriguez et al. 2020], generate hail and lightning (Fromm et al. 2006, 2010; LaRoche and Lang 2017), and spawn tornadic vortices (Fromm et al. 2006; Cunningham and Reeder 2009; McRae et al. 2013; Lareau et al. 2018). Recent exemplars of these extremes include California's Carr Fire in 2018, which produced pyroCb and a deadly pyrogenetic tornado with winds > 140 mph (Lareau et al. 2018), and the Loyalton Fire in 2020, which necessitated the first-ever National Weather Service (NWS) fire tornado warning (Cappucci 2020).

Despite their impacts, the dynamics of fire-generated tornadic vortices (FGTVs) are not well established, having only been comprehensively documented in two cases to date (Fromm et al. 2006; McRae et al. 2013; Lareau et al. 2018). For example, it is not understood where in the fire FGTVs form, how they are linked to the convective plume and vigorous pyroconvection, including pyroCb, and how consistent their radar signatures are from one event to the next. This knowledge gap motivates this paper, which establishes commonalities in the location, morphology, and evolution of FGTVs during three high-impact wildfires.

Understanding vortices generated by fires

Fire-generated vortices (FGVs) span many spatial, temporal, and intensity scales (Forthofer and Goodrick 2011; Tohidi et al. 2018). While FGVs can have both vertical and horizontal axes of rotation (e.g., fire-whirls versus horizontal roll vortices; Haines and Smith 1987), the focus of this study is on FGVs with predominantly vertical axes. Small FGVs (~10 m) are common and transient (tens of seconds), often presenting as flaming upright whirls along the fire line, whereas larger, long-lived FGVs (~100 m, tens of minutes) are less common, but still regularly observed by firefighters (Countryman 1971). In contrast, FGTVs (also called pyrogenetic tornadoes; Cunningham and Reeder 2009) are exceedingly rare, with winds as high as 62 m s⁻¹ (140 mph), vertical extents of thousands of meters, large diameters (100–1000 m), and dynamical links to the updrafts in deep pyroconvection, including pyroCb (Fromm et al. 2006; Cunningham and Reeder 2009; McRae et al. 2013; Lareau et al. 2018).

The spectrum of FGV spatial and intensity scales, up to and including FGTVs, suggests a range of governing processes and vortex morphologies. Indeed, experiments and observations indicate multiple types of vortices occur in wildfire (or other) convective plumes (e.g., Church et al. 1980; Fric and Roshko 1994; Cunningham et al. 2005). Excellent reviews of FGVs are available from Forthofer and Goodrick (2011) and Tohidi et al. (2018). Some key elements of plumes and vortices particularly relevant to our FGTV cases are summarized below.

Plumes in a cross flow. Experiments with jets/plumes in a cross flow, analogous to a wild-fire convective plume in a background wind, indicate counterrotating vortex pairs (CVPs), near-surface flow splitting and reversal, and wake vortices that detach from the plume and migrate downstream (Mahesh 2013). Figure 1 provides an annotated summary of some of these plume, vortex, and flow features, which are elaborated on below.

The CVP is *embedded* within the jet/plume core with the axis of rotation parallel to the jet/plume trajectory and thus near vertical close to the origin and quasi-horizontal downstream (red and blue arrows, Fig. 1a). Examples of CVPs in wildfire scenarios include those in simulations by Cunningham et al. (2005) and Thurston et al. (2017) and in observations from Church et al. (1980), Haines and Smith (1987), and Banta et al. (1992). Based on inferences from open-flame experiments Shinohara and Matsushima (2012) hypothesize that CVPs may be the source of large FGVs in landscape-scale fires (i.e., thousands of acres).

Jets/plumes in a cross flow also yield flow splitting around the jet core, with enhanced flow around the jet's periphery and reversed flow in the jet's lee, implying counter rotation associated with the CVP (Fig. 1b). This pattern can become asymmetric for oval jets at an angle to the flow (Wu et al. 1988; Fig. 1c) and due to sheared wind profiles (Lavelle 1997). Flow splitting and flow reversal are apparent in coupled fire—atmosphere simulations with more complex fire-line geometry (Clark et al. 1996) and have long been postulated as being associated with FGVs (tornadic and otherwise), such as discussed by Countryman (1971) and echoed in Forthofer and Goodrick (2011) and Potter (2012).

Wake vortices (a.k.a. shedding vortices) are "tornado-like," originate near the leeside of the jet/plume, occur in alternating cyclonic and anticyclonic patterns, and remain pendant from the bent-over plume (red and blue shading, Fig. 1a). Their formation is sensitive to the comparative strength of the jet/plume updraft and that of the cross-flow (Fric and Roshko 1994). Wake vortices have been observed in man-made fires (Church et al. 1980), are apparent in numerical simulations of wildfire plumes (Cunningham et al. 2005), and are likely implicated in destructive vortices documented during wildland and industrial fires (Pirsko et al. 1965; Hissong 1926).

Pyrocumulonimbi. Vigorous pyroconvection, including pyroCb, appears to be linked to FGTV formation and intensification (Lareau et al. 2018). PyroCb form when fire-generated updrafts reach their level of free convection (LFC), release moist instability aloft, and then rise

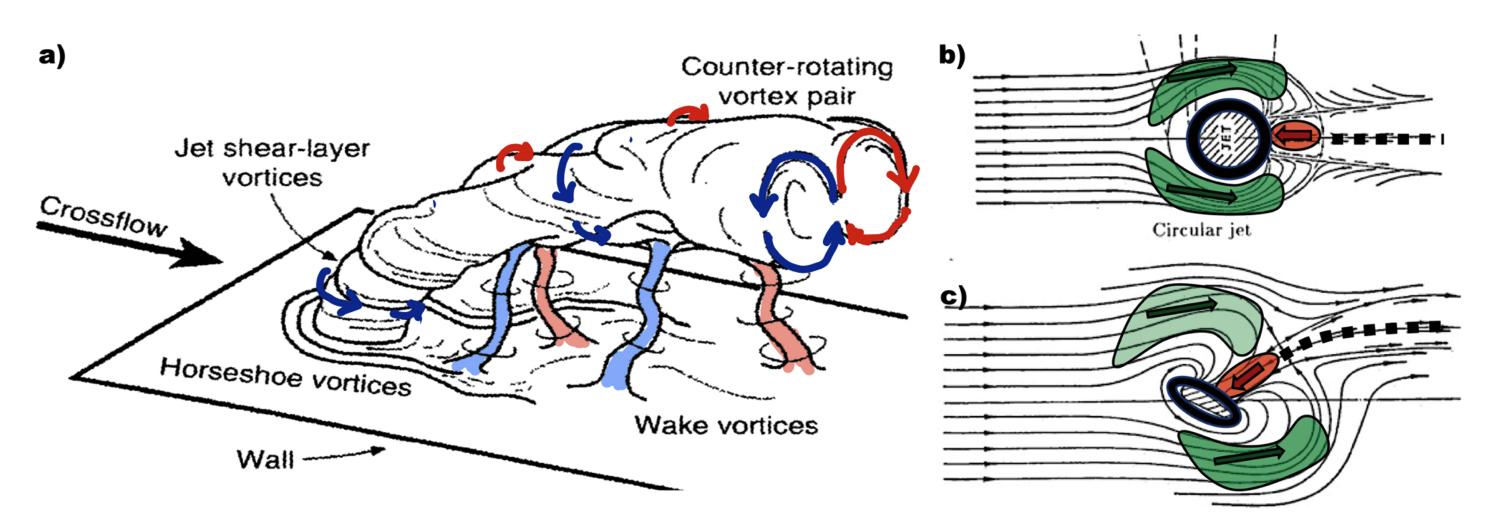


Fig. 1. Schematic of vortex, plume, and flow structures observed in laboratory experiments with jets in a cross flow, reproduced from (a) Fric and Roshko (1994) and (b),(c) Wu et al. (1988). Annotations have been added by the authors. (a) Bent-over plume in a cross flow exhibiting a counterrotating vortex pair (red and blue arrows) and wake vortices (red and blue shading). (b),(c) Flow features around the base of (b) circular and (c) oval jets at an angle to the flow. Colored annotations emphasize the flow splitting (green), flow reversal (red), and wake (black dashed line) regions.

above the homogenous freezing level (–38°C; Fromm et al. 2010). A fire's ability to reach the LFC is a function of the thermodynamic environment (Lareau and Clements 2016; Peterson et al. 2017a,b; Rodriguez et al. 2020), the fire's sensible and latent heat fluxes (Trentmann et al. 2006; Luderer et al. 2006, 2009; Tory et al. 2018; Tory and Kepert 2021), and the size/geometry of the fire (Badlan et al. 2021a,b). PyroCb cloud base tends to occur near the convective condensation level (CCL; Lareau and Clements 2016), and more precisely is determined by the plume's temperature and moisture (Tory et al. 2018). Updrafts near pyroCb cloud base can be as high as 60 m s⁻¹ (Rodriguez et al. 2020) and plume tops can penetrate the stratosphere (Fromm et al. 2006, 2010; Peterson et al. 2021). Accordingly, vigorous pyroconvection, including pyroCb, have been linked to violent firestorms (Fromm et al. 2006; Peterson et al. 2015; Peace et al. 2017; Terrasson et al. 2019) and FGTVs, wherein it is hypothesized that pyroCbs provide enhanced column stretching that contributes to FGTV spinup (Cunningham and Reeder 2009; McRae et al. 2013; Lareau et al. 2018).

While there are strong indications that "jet in a crossflow" dynamics and vigorous pyroconvective processes both contribute to FGTV development, to date there have been few observations of vortex and plume morphology with which to confront these theories. This sets the stage for the analyses that follow.

Identifying and characterizing FGTVs

Radar data. NEXRAD radar data are used to quantify wildfire plume processes, including FGTV winds. These 10-cm-wavelength radars are sensitive to the large (millimeter to centimeter scale) particulate ash and debris, called pyrometeors, lofted in wildfire convective plumes (McCarthy et al. 2019). The metadata for the radars used are included in Table 1. For analyses of three-dimensional plume structures these radar data are interpolated to common Cartesian grids whereas for analyses of the near surface winds data are kept on a native polar grid (azimuth, range). Some of the velocity data are aliased, requiring an algorithmic and manual dealiasing (see online supplemental material text).

After dealiasing, FGTV strength is quantified using the rotational velocity, given by

$$V_{\rm rot} = \frac{1}{2} (V_x - V_n),$$

where V_x and V_n are the strongest out/inbound radial velocities, respectively, proximal to the vortex center, which is manually determined (Gibbs 2016). V_{rot} is correlated with, but different from, the actual vortex strength. Due to the need for dealiasing there is some uncertainty in the V_{rot} values. Examples of the dealiasing and its uncertainties are available in the supplemental material text.

Satellite data. Data from *GOES-17* are used to examine fire and plume processes. We use a "Fire-RGB" approach, which blends data from the near-infrared (1.6, 2.2, 3.9 μ m) channels and allows viewers to differentiate between more and less intense fires (red is cooler, white is

Table 1. Metadata for NEXRAD radar sites.

Radar site	Radar ID	Fire(s) observed	Location (lat, lon)	Base elevation	Volume coverage pattern	Nyquist velocity	Approx distance to fire	Azimuthal resolution near FGTVs
Reno, NV	KRGX	Loyalton, Creek	39.7542°, –119.4622°	2530 m MSL	12	23.6 m s ⁻¹ (45.9 kt)	55 km	480 m
Beale Air Force Base, CA	KBBX	Bear	39.4961°, –121.6317°	53 m MSL	32, 215	27.88 m s ⁻¹ (54.2 kt)	43 km	375 m
Hanford, CA	KHNX	Creek	36.3142°, –119.6322°	74 m MSL	215	24.18 m s ⁻¹ (47 kt)	115 km	1 km
Sacramento, CA	KDAX	Creek, Bear	38.5011°, –121.6778°	9 m MSL	35	Not used for velocity data	144 km (Bear) 238 km (Creek)	1.25 km 2 km

hotter; https://rammb.cira.colostate.edu/training/visit/quick_guides/Fire_Temperature_RGB.pdf). Similarly, we use "true-color RGB" imagery to examine smoke and pyroCb processes. The true-color images combine data from the 0.47 μ m (blue), 0.64 μ m (red), and 0.86 μ m ("veggie") channels. The spatial resolution of the fire- and true-color-RGB data are 2 and 1 km, respectively.

Ancillary data. Data from the High-Resolution Rapid Refresh (HRRR; Benjamin et al. 2016) hourly analyses are used to characterize the meteorology during the FGTVs. These data include the near-surface wind (80 m AGL), midtropospheric wind (700, 500 hPa), 500-hPa geopotential heights, and gridpoint thermodynamic profiles. Thermodynamic data from the Reno, Nevada, radiosonde are also used in the case study of the Loyalton Fire. Fire perimeter data are obtained from the National Infrared Observations (NIROPS) program.

EMBEDDED AND SHEDDING VORTICES DURING THE LOYALTON FIRE. The lightning started Loyalton Fire consumed ~20,000 acres (8,100 ha) on 15 August 2020, yielding a deep pyroCb and a sequence of FGTVs (Table 2). The fire's growth occurred during southwest surface winds, which backed with height, becoming more southerly in the midtroposphere (Fig. 2c). The thermodynamic environment was conducive to elevated convection (Figs. 2a,d) and consistent with the climatology of pyroCb environments (Peterson et al. 2017a). Namely, there is a deep, dry, well-mixed layer extending from the surface to ~550 hPa, which is conducive to active fire behavior and vertical plume development, overtopped with a moist mid- to upper troposphere, which is supportive of moist convection.

The evolution of the Loyalton Fire's FGTVs and pyroCbs are summarized in Fig. 3 (also see supplemental animation S4.gif). The time—height diagram of radar reflectivity (Fig. 3a) indicates rapid plume growth from 6.5 to ~13 km MSL. During the plume deepening, cores of high-reflectivity air (>30 dBZ) ascend with time, indicative of vigorous convective updrafts. Noting that the CCL was at ~5 km (black dashed line in Fig. 3a), the entire upper portion of the plume was involved in deep-moist convection, as is apparent from photographs (Fig. 3c) and satellite imagery (Fig. 3d). The plume tops extended above the homogenous freezing level (–38°C at 10.1 km), ensuring a glaciated pyroCb. The cloud top was close to the tropopause, which had a double structure with tropopause features at both 13,638 and 15,847 m.

During the plume growth a sequence of anticyclonic FGTVs developed, as shown in the time series of $V_{\rm rot}$ (Fig. 3b) and vortex depths (black squares, Fig. 3a). These data show long-duration vortex activity, punctuated by periods with peak $V_{\rm rot}$ reaching as high as 25.5 m s⁻¹ (~50 kt). The $V_{\rm rot}$ was strongest close to the surface and decayed with height. The corresponding vortex depths were notable, with one vortex (~2035 UTC) reaching ~6.5 km MSL (4.9 km AGL), and multiple vortices extending above the condensation level (see supplemental material text). This means that some, but not all, of the vortices extend from the surface into the pyroCb.

Table 2. Summary of fire information.

Fire name	Location (lat, lon)	Start date	Analysis date(s)	Acres burned on day of FGTVs	Total acres	Fuels	Inciweb link
Loyalton	39.681°, –120.171°	14 Aug 2020	15 Aug 2020	20,000	47,029	Timber, sage, tall grass	https://inciweb.nwcg.gov/incident/6975/
Creek	37.201°, –119.272°	4 Sep 2020	5 Sep 2020	45,531	379,895	Mixed conifer, grass and oak woodlands, shrubs/brush	https://inciweb.nwcg.gov/ incident/7147/
Bear/North Complex	40.091°, –120.931°	17 Aug 2020	8–9 Sep 2020	193,759	318,935	Mixed conifer, brush	https://inciweb.nwcg.gov/ incident/6997/
King	38.782°, –120.604°	13 Sep 2014	17 Sep 2014	50,014	97,717	Mixed conifer	_
Apple	33.998°, –116.933°	31 Jul 2020	2 Sep 2020	20,000	33,424	Chaparral and Brush	https://inciweb.nwcg.gov/ incident/6902/

Loyalton Fire 08/15 2100-2200 UTC Avg.

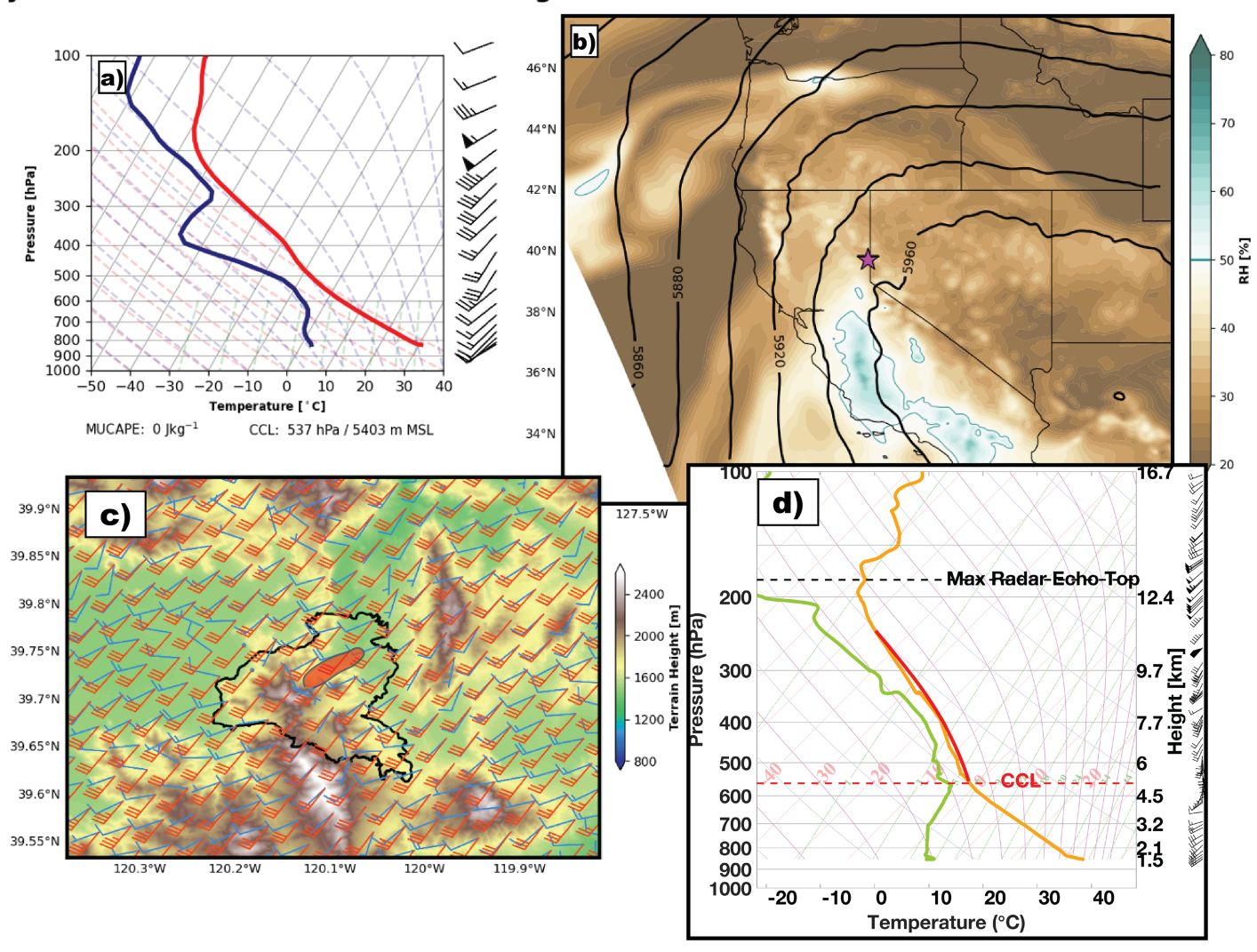


Fig. 2. Overview of the meteorology during the Loyalton Fire on 15 Aug 2020. (a) HRRR model sounding; (b) 500-hPa heights (in m) and 700–400-hPa layer-averaged relative humidity (shading); (c) wind barbs for near-surface (blue) and 500-hPa (red) winds along with the fire perimeters (black line), approximate vortex zone (red shaded), and topography (shaded); and (d) KRNO sounding at 0000 UTC on 16 Aug showing the convective condensation level (CCL), radar-estimated plume tops (black dashed line) and estimated parcel ascent from the CCL (red line).

Radar snap shots of the strongest vortices at 2030, 2125, and 2205 UTC (Fig. 4) indicate distinct in- and outbound velocity couplets (Figs. 4b,d,f) near the advancing left flank of the head fire (black dashed lines; Figs. 4a,c,e). These radar data are from KRGX's second-lowest scan elevation (0.5°), yielding 500–1500 m AGL radar beam heights in the vicinity of the FGTVs. The first two FGTVs were anchored to the head fire and reside within high-reflectivity updraft cores (Figs. 4a–d; see also supplemental animation S2mov.mp4). In contrast, the third vortex was detached from the fire, residing in a lower-reflectivity region downstream (i.e., to the northeast; Figs. 4e,f; see also supplemental animation S3mov.mov).

These vortex locations are representative of two distinct vortex morphologies linked to persistent flow features, as revealed by a time-mean analysis (Figs. 5a,b). To be specific, flow splitting (blue arrows, Fig. 5b) and reversal (red arrow, Fig. 5b) occur around the edges of, and in the lee of, the high-reflectivity updraft core rising from the head fire (black oval, Fig. 5a). This persistent flow pattern implies a CVP linked to the fire flanks (red and blue circles, Fig. 5b).

The vortex core locations (triangles) indicate two groupings related to these flow features. The first (red triangles) reside in the high-reflectivity updraft and within the anticyclonic branch of the broader CVP, and thus constitute *embedded* vortices, which might also be

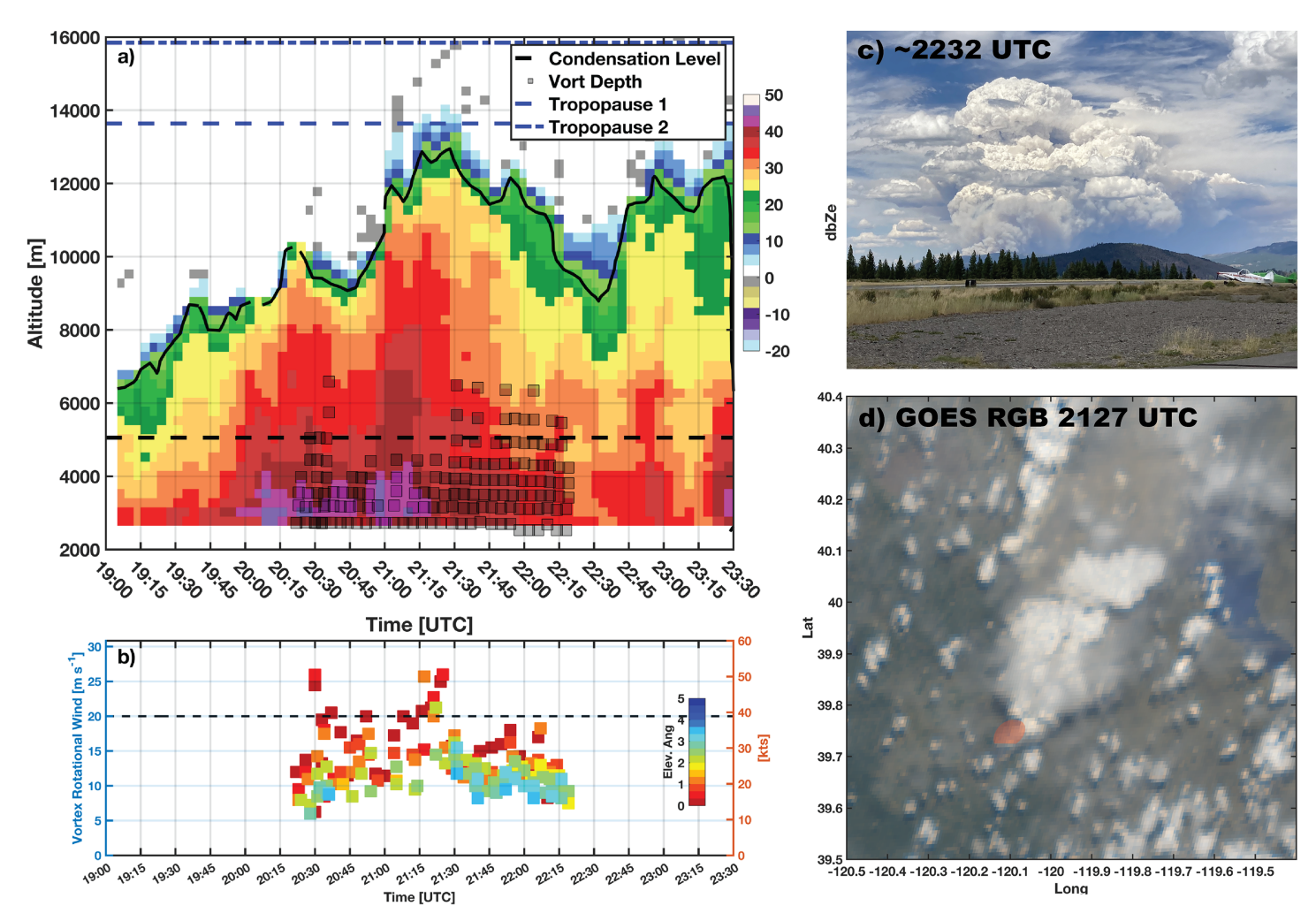


Fig. 3. Overview of the Loyalton Fire's plume growth and FGTV generation. (a) Radar reflectivity time–height diagram showing the plume tops (black line), estimated CCL (black dashed line), tropopause heights (dashed blue, note double tropopause), and the vortex vertical extents (black squares). (b) Time series of the rotation velocity (m s⁻¹ on left axis, kt on right axis) for different radar elevation scans (colors). The black dashed line indicates the 20 m s⁻¹ line, which is linked to intense vortices. (c) Photograph of the Loyalton Fire's pyroCb looking NNE from Truckee, CA (photo credit: Alex Neigher). (d) *GOES-17* true-color image of the pyroCb with a red area denoting the approximate fire footprint.

described as helical updrafts. The second subset (purple triangles) are *shedding* vortices and are found downwind from the primary fire front (though they may carry flames and embers with them), where they progress along the anticyclonic shear zone on the periphery of the flow reversal region. The shedding vortices in this case traveled \sim 7 km over the course of 1 h, yielding an average translation speed of 1.2 m s⁻¹.

These FGTV and plume morphologies are also apparent in the 3D plume structure, as shown with radar reflectivity isosurfaces and vertical vortex lines (Figs. 5c,d). These data indicate that the convective plume is bent over in the wind, with evidence for bifurcation (see P1 and P2 plume cores in Fig. 4d) associated with the CVP. The embedded vortices reside within the high-reflectivity updraft (P1). The shedding vortices detach from the updraft and translate downwind, pendant from the underside of the arcing plume in a region of low reflectivity. Thus, even if the shedding vortex contains fire and embers, it has separated (i.e., shed) from the fire's primary updraft. This region of low reflectivity is also apparent as the narrow "weakness" in the reflectivity plan-view map in Fig. 5a, which occurs in the region between the updraft and the ash fall downwind. The time mean radar reflectivity also indicates a counterclockwise curving ashfall region (black dashed line, Fig. 5a), which is evidence of the backing wind profile (shown in Figs. 2a,c,d).

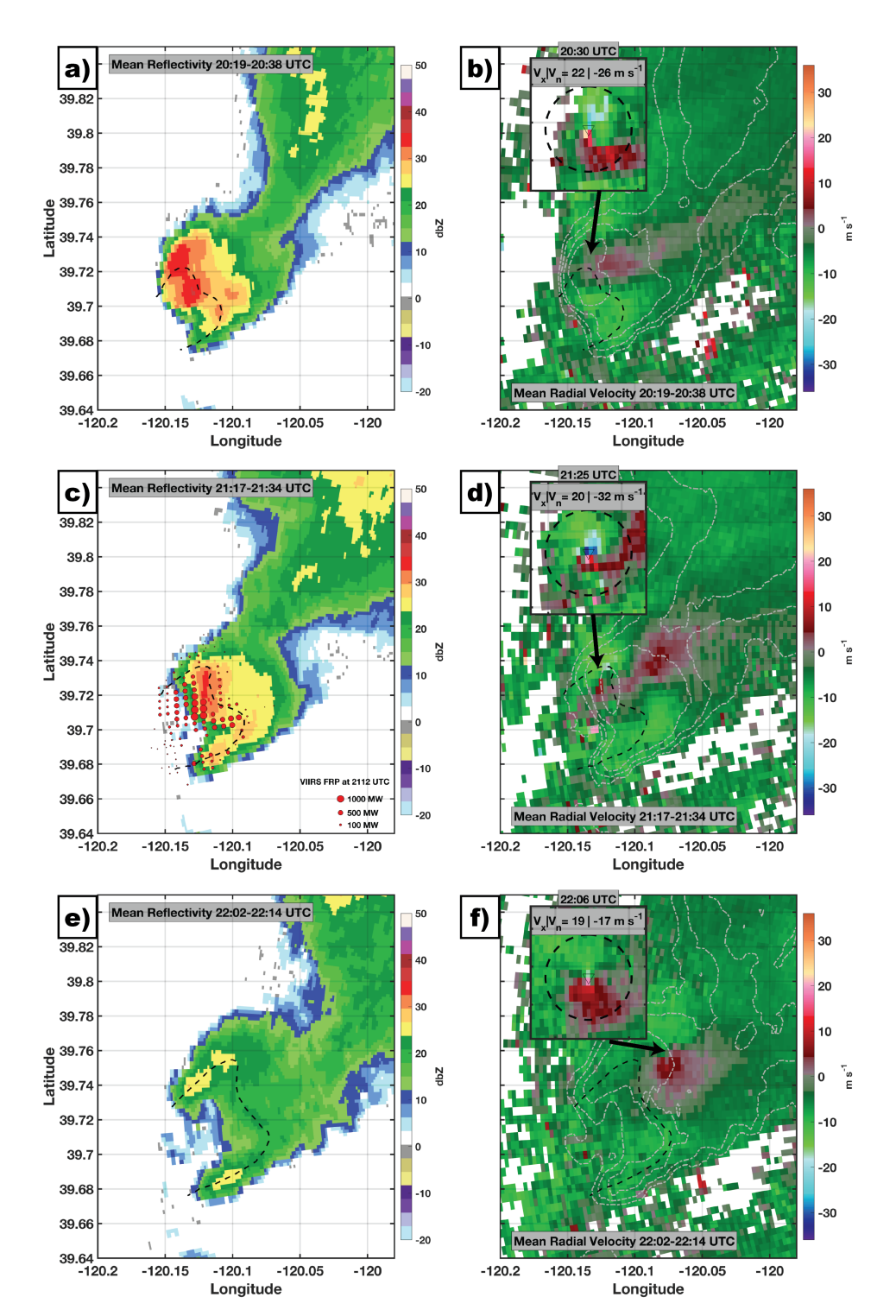


Fig. 4. Overview of radar signatures linked to intense FGTVs during the Loyalton Fire from the 0.5° beam from KRGX. (a),(c),(e) Radar reflectivity and (b),(d),(f) radial velocity data averaged for the times surrounding the most intense FGTVs. The fire perimeter is approximated (black dashed line) and the FGTV vortex signature is shown in the inset. The VIIRS fire detections at 2112 UTC are shown in (c), with marker size corresponding to the FRP, as shown in the scale. The green and red colors are flow toward and away from the radar, respectively. The maximum in- and outbound flows are shown. The height of the radar beam above ground level in the vortex locations ranges from 500 to 1500 m.

Photographs and videos help confirm these radar observations, showing that the earlier FGTVs (e.g., before 2130 UTC) were embedded in an anticyclonically rotating smoke and ash filled convective column linked directly to the fire (P1, Fig. 5e; also see supplemental

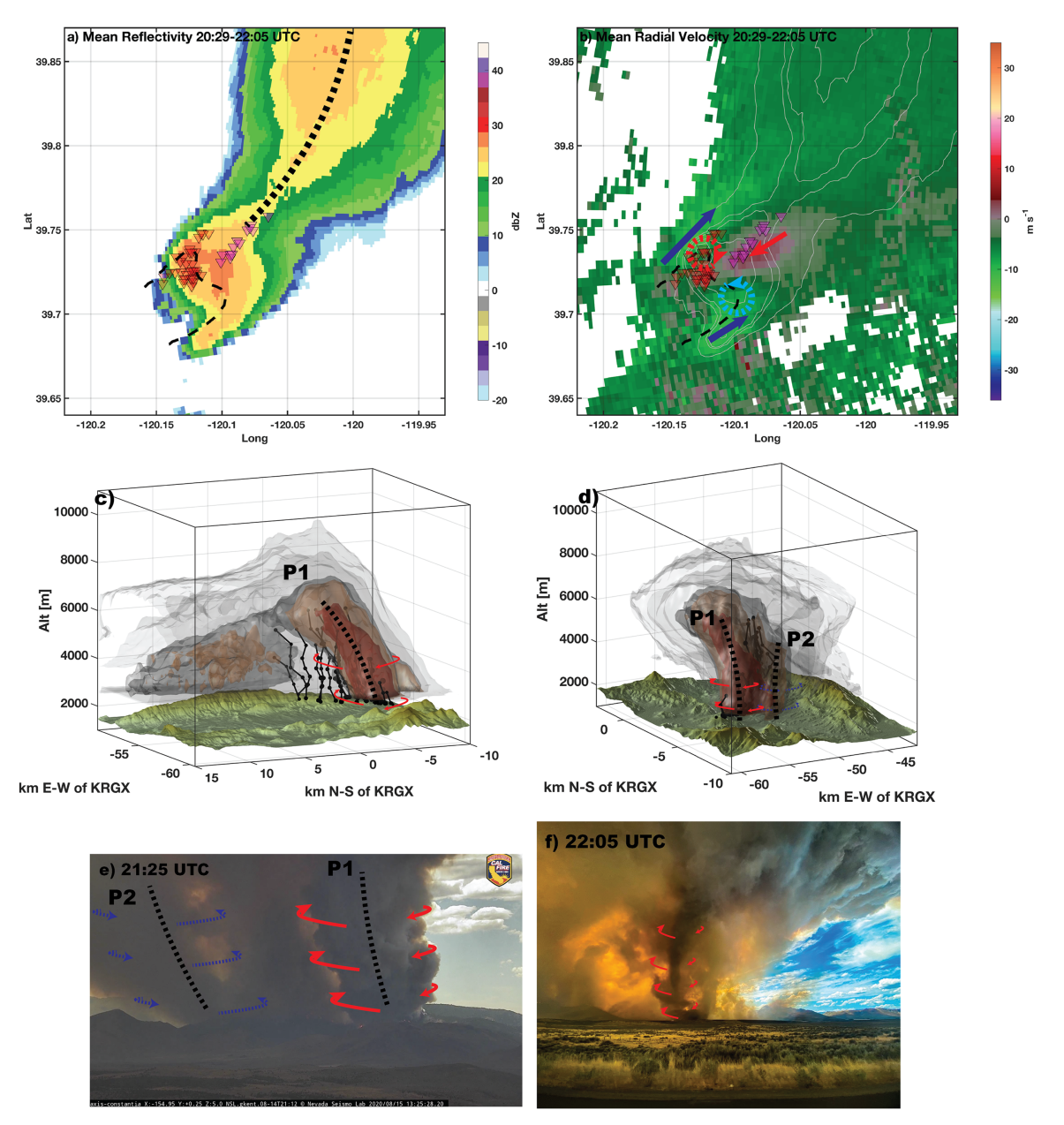


Fig. 5. Summary of vortex morphologies and locations. (a),(b) Time-averaged radar reflectivity and radial velocity with vortex locations (triangles). Red triangles indicate embedded vortices and magenta triangles indicate shedding vortices. Blue and red arrows show the flow splitting and reversal features, respectively, and red and blue dotted circles with arrows show the location of the counter-rotating vortex pair. (c),(d) Radar reflectivity isosurfaces showing the time-averaged plume structure from (c) the northwest and (d) the southwest. The solid black lines and filled circles indicate vortex lines, with the marker size scaled to the rotational velocity. The annotations (P1, P2) show two distinct, bifurcating plume cores, whose sense of rotation is indicated with colored arrows. (e),(f) Photographs of the (e) embedded vortices within the dominant anticyclonic branch (P1, red arrows; courtesy of CalFire and AlertWildfire) of the counter-rotating vortex pair and (f) shedding vortices (photo credit: Jordan Hewlett). Both photographs are taken from the northeast looking approximately along the mean wind.

animation S2mov.mp4). In contrast, the later "shedding" FGTV, shown in Fig. 5f, was funnel-like, pendant from the plume aloft, and separated from the primary fire front, consistent with the 3D radar renderings (see also supplemental animation S3mov.mov).

Taken together, the observations from the Loyalton Fire provide rare insight into the location and morphology of FGTVs and show distinct similarities to laboratory experiments with jets/plumes in crossflows in terms of vortex locations, flow features, and plume geometry (cf. Fig. 1).

LARGE EMBEDDED VORTICES DURING THE CREEK FIRE. The Creek Fire generated explosive pyroCb activity, with cloud tops reaching ~16 km MSL, and multiple strong FGTVs (30 m s⁻¹) on 5 September 2020 under the influence of diurnally varying upslope and upvalley winds (Fig. 6c, Table 2). Like the Loyalton Fire, a pronounced backing wind profile impacted the plume (Figs. 6a,c,d), whose growth is summarized in Fig. 7 (see supplemental animation S5.gif). These data indicate progressive plume deepening (from 8 to ~16 km), periods with deep convective cores, and sustained pyroCb activity (as shown in Figs. 7c,d). Plume tops easily surpassed the CCL at ~5.9 km and the homogenous freezing level at ~11 km. The cloud tops were close to the tropopause height, which was ~16,800 m, as determined from a sounding at Reno, NV. The pyroCb went on to produce lightning, precipitation, and downdrafts (a complete analysis of which are beyond the scope of this manuscript). These radar data also indicate a secondary pyroCb event in the evening (~0245 UTC 6 September) wherein high-reflectivity cores (~40 dBZ) reached ~12 km and plume tops 14 km.

The $V_{\rm rot}$ time series (Fig. 7b) and vortex depths (black squares, Fig. 7a) show that the three deepest plume pulses were associated with FGTVs with $V_{\rm rot}$ exceeding 20 m s⁻¹ (40 kt) at ~2050, 2200, and 0310 UTC (6 September). The peak $V_{\rm rot}$ twice reached 30 m s⁻¹ (60 kt, see also supplemental text), which is ~5 m s⁻¹ (10 kt) stronger than in the Loyalton Fire

Creek Fire 09/05 2000-2200 UTC Avg.

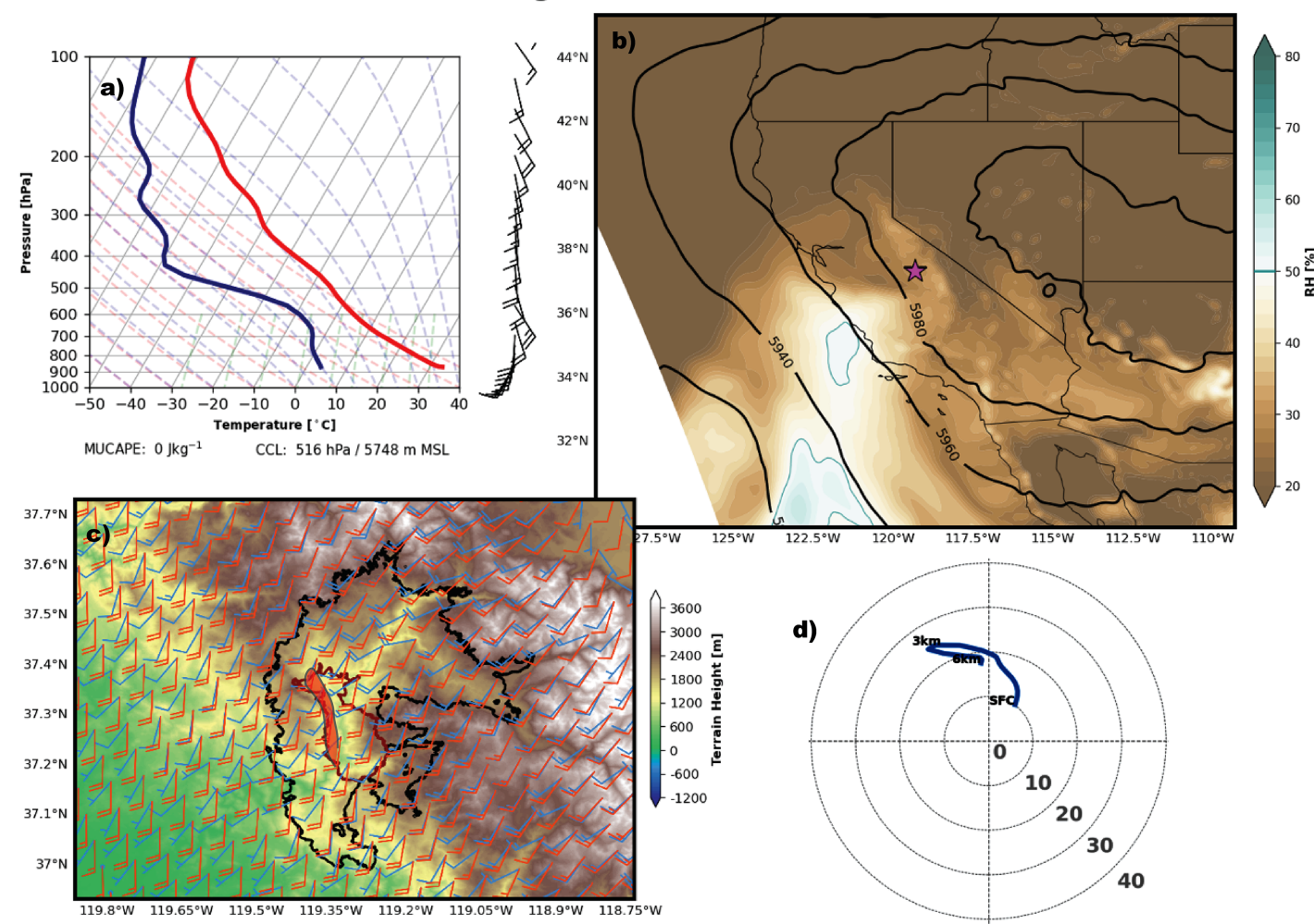


Fig. 6. Overview of the meteorology during the Creek Fire on 5 Sep 2020. (a) HRRR model sounding; (b) 500-hPa heights (in m) and 700–400-hPa layer-averaged relative humidity (shading); (c) wind barbs for the surface (blue) and 700 hPa (red), approximate vortex zone (red shading), fire perimeters (black line is the final perimeter, maroon line the perimeter at ~0500 UTC 6 Sep 2020) and topography (shaded); and (d) hodograph showing the change in wind speed and direction with height.

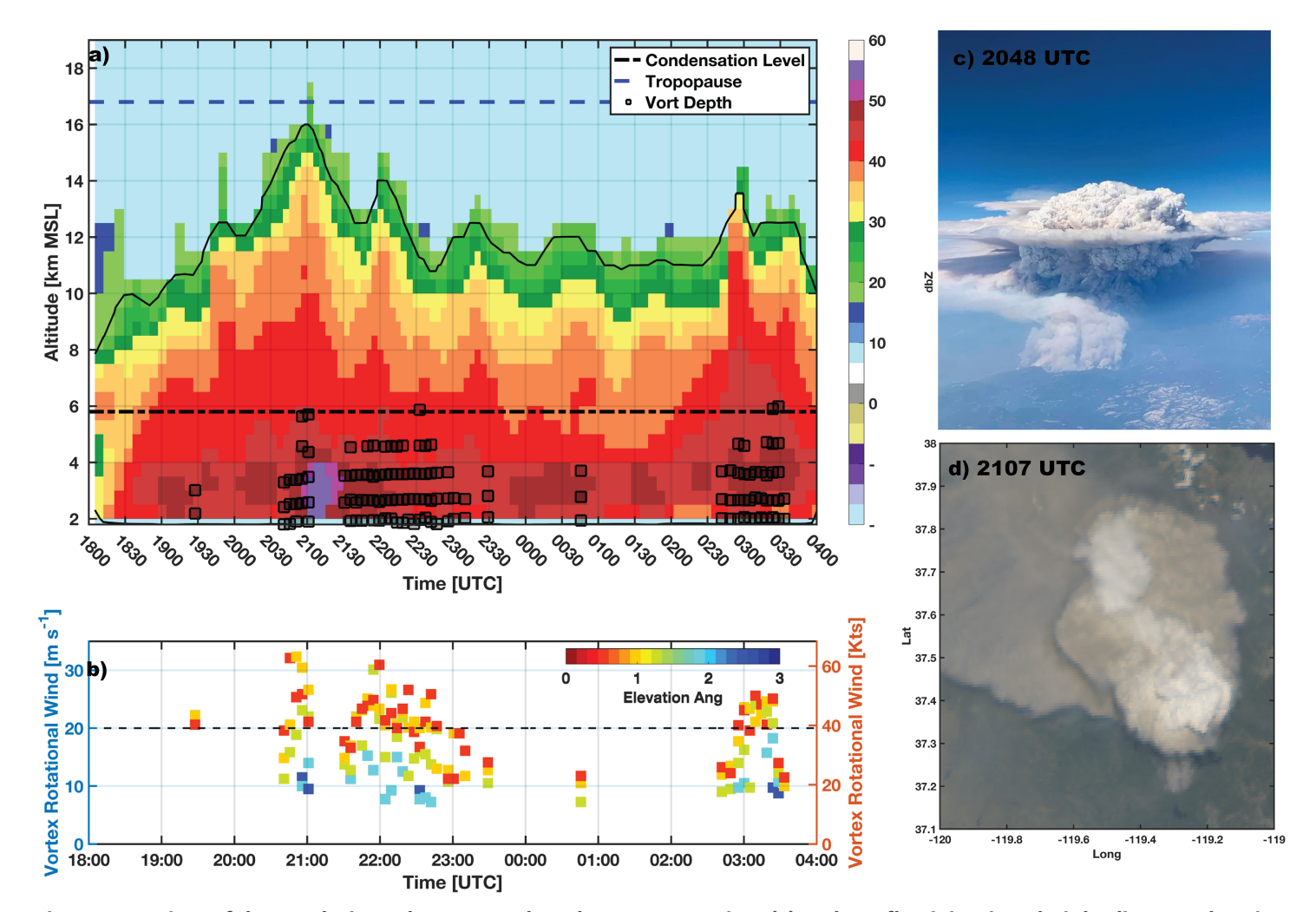


Fig. 7. Overview of the Creek Fire's plume growth and FGTV generation. (a) Radar reflectivity time–height diagram showing the plume tops (black line), estimated CCL (black dashed line), tropopause height (blue dashed line), and the vortex vertical extents (black squares). (b) Time series of the rotation velocity (m s⁻¹ on left axis, kt on right axis) for different radar elevation scans (colors). The black dashed lines indicates the 20 m s⁻¹ line, which is linked to intense vortices. (c) Photograph of the Creek Fire pyroCb (photo credit: Thalia Dockery). (d) *GOES-17* true-color image of the pyroCb.

despite the diminished beam-to-beam azimuthal resolution (1 km versus 480 m, see Table 1). The corresponding vortex depths (black squares in Fig. 7a) indicate vertically continuous circulations from the surface (\sim 1,500 m) to \sim 6 km MSL. Based on the estimated CCL (5.9 km), it is likely that some of these vortices extended to cloud base.

The Creek Fire's FGTVs were all anticyclonic, occurring on the advancing left flank of the head fire (Figs. 8a–i), in a location conspicuously similar to the FGTVs during the Loyalton Fire. Notably, the FGTV location is persistent in time and space *relative* to the fire throughout the day, implying these vortices are anchored to, and *embedded* in, the fire's updrafts (i.e., helical updrafts). The radar snap shots additionally show that the width of the anticyclonic circulation is much larger during the Creek Fire (~5-km diameter) than during the Loyalton Fire (~1–2-km diameter). These broader circulations suggest the potential for more significant wind impacts.

Apart from the FGTVs, the radar-observed airflow indicates prominent flow splitting around the fire flanks (red) and flow reversal zones (green) downwind of the head fire (Figs. 8b,e,h). The flow reversal is most pronounced at ~2200 UTC, extending ~10 km downwind of the head fire and reflecting a meso-gamma-scale modification of the ambient flow due to the fire's updraft (Fig. 8e). As with the Loyalton Fire, this flow reversal region is distinct from the FGTV circulation and is present even at times when no FGTV is observed.

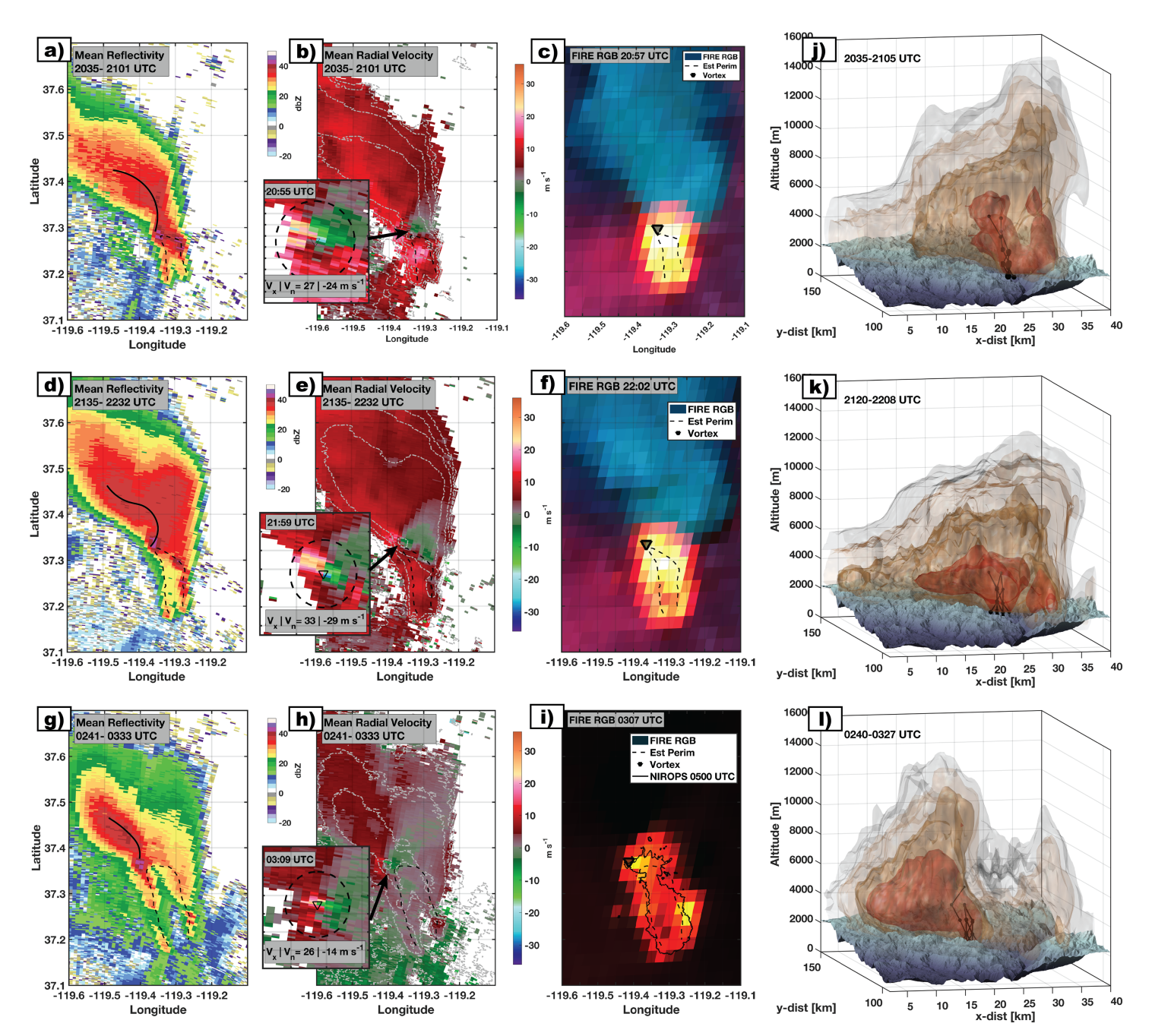


Fig. 8. Overview of intense FGTVs during Creek Fire. (a),(d),(g) Radar reflectivity and (b),(e),(h) radial velocity data averaged for the times surrounding the most intense FGTVs. The fire perimeter is approximated (black dashed line) and the most intense FGTV signature is shown in the inset. The green and red colors are flow toward and away from the radar, respectively. (c),(f),(i) Fire–RGB satellite imagery showing the fire location and relative intensity along with estimated fire perimeters and FGTV locations. (j),(k),(l) Radar reflectivity isosurfaces of the time-averaged plume structure looking from the southwest. The solid black lines and filled circles indicate vortex lines, with the marker size scaled to the rotational velocity.

The radar reflectivity and velocity signatures are suggestive of mesocyclonic storm structures during ordinary tornados (Figs. 8a,d,g). To be specific, the FGTVs are collocated with quasi-circular maxima in radar reflectivity, indicative of heavy ash and debris loading. Downwind of the FGTV maxima, the ash fall region exhibits a counterclockwise turning (solid black lines) indicative of the backing wind profile (e.g., hodograph in Fig. 6d). The backing winds result from a combination of thermally forced upslope and upvalley winds at the surface and a southeasterly flow aloft around an anomalous upperlevel ridge to the East (Fig. 6b)

The FGTV relationship to the three-dimensional plume structure is examined using radar reflectivity isosurfaces and vortex lines (Figs. 8j,k,l). These data show that during the initial vortex phase (2030–2100 UTC) there are two distinct plume cores (i.e., bifurcating plume) on the left and right flanks of the head fire (Fig. 8j). The anticyclonic vortices are *embedded* in the left, shallower updraft and ascend to ~5 km MSL. Interestingly, the right (cyclonic) updraft is linked to the much deeper part of the plume, which reaches ~16 km MSL.

During the second vortex period (2130–2158 UTC) the plume cores have moved laterally away from one another, and the left (anticyclonic) plume is more bent over, while the cyclonic updraft remains more upright and deeper (Fig. 8k). As before, the vortex cores remain embedded in the anticyclonic updraft. In contrast, for the tertiary, nocturnal FGTV (0240–0327 UTC) the cyclonic updraft is less established, and the deepest part of the plume is linked to the anticyclonic vortex region (Fig. 8l). One reason for this change may be decoupling of the near-surface winds after dark (note inbound flow adjacent to the fire in Fig. 8h).

In summary, the Creek Fire produced long-duration, high rotational velocity, *embedded* vortices linked to an extremely deep pyroCb. Like the Loyalton Fire, flow reversal and flow splitting due to the fire's updraft are prominent manifestations of fire-modified flows. However, unlike the Loyalton Fire, all FGTVs remained embedded within updraft cores, with no indication of vortex shedding.

Shedding vortices during the Bear Fire. Whereas the Loyalton and Creek Fires occurred under typical summer conditions, the Bear Fire (Table 2) occurred during a strong downslope windstorm (Fig. 9), with sustained northeast winds of 15 m s⁻¹ (Fig. 9c) and gusts up to 30 m s⁻¹ (Fig. 9d). These winds drove rapid fire spread and contributed to substantial temporal variations in plume depth (Fig. 10a; see supplemental animation S6.gif), including "pyropulses" wherein short duration pyroCb developed, then dissipated. The estimated cloud base was >6 km MSL and the homogeneous freezing level ~10 km MSL. The tropopause during the Bear Fire exhibited a double structure, with temperature inversions at $\sim13,300$ and $\sim15,550$ m.

The period of interest for FGTVs is the pyropulse reaching ~12 km at 0040–0200 UTC (Figs. 10a,c). During this time a sequence of short-lived, intense, anticyclonic vortices were observed, as shown in the $V_{\rm rot}$ time series (Fig. 10b). The strongest FGTV reached a $V_{\rm rot}$ of 30 m s $^{-1}$ (60 kt) with a depth of 3.3 km MSL. Despite the separation between the vortex tops and the cloud base (>6 km), there is a clear covariation of pyroCb depth and FGTV strength (Fig. 10b). This covariation occurs with both the spinup and spindown, as evident in the decrease in vortex depth and rotation as the pyroCb plume tops subside from 0100 to 0200 UTC. We note that the Loyalton and Creek Fire cases showed similar covariations in plume and vortex processes, as did the Carr Fire (Lareau et al. 2018), suggesting vortex tube stretching via plume vertical development. This covariation also suggests feedbacks between the vortex and plume development, which may occur due to enhanced buoyancy and updraft speeds in the vortices due to decreased entrainment into the rotating flow (e.g., cyclostrophic flow; Tohidi et al. 2018).

Time-averaged radar maps, along with vortex snapshots, establish the dominant flow features during the Bear Fire (Figs. 11a,b). Like the previous fires, these data indicate prominent flow reversal (red shading) extending >10 km downwind of the head fire, with strong convergence between the northeasterly winds $(15-25 \text{ m s}^{-1})$ and the reversed flow $(10-15 \text{ m s}^{-1}; \text{ Fig. 11b})$. The northeasterly flow splits around the head fire, yielding cyclonic and anticyclonic shear zones along the northern and southern periphery of the flow reversal zone, respectively. The anticyclonic shear zone is the stronger of the two (i.e., a tighter gradient), and hosts the compact, but vigorous, anticyclonic FGTVs (Figs. 11c-e). The radar snapshots also show that the FGTVs emerge from near the head fire, then migrate downstream along the anticyclonic shear maxima (Figs. 11c-e). The first FGTV traveled ~2.1 km in 20 min yielding a translation speed of ~1.75 m s⁻¹. The second FGTV traveled further and faster, moving ~4.2 km in 17 min, yielding a speed of

Bear Fire 09/09 0000-0200 UTC Avg.

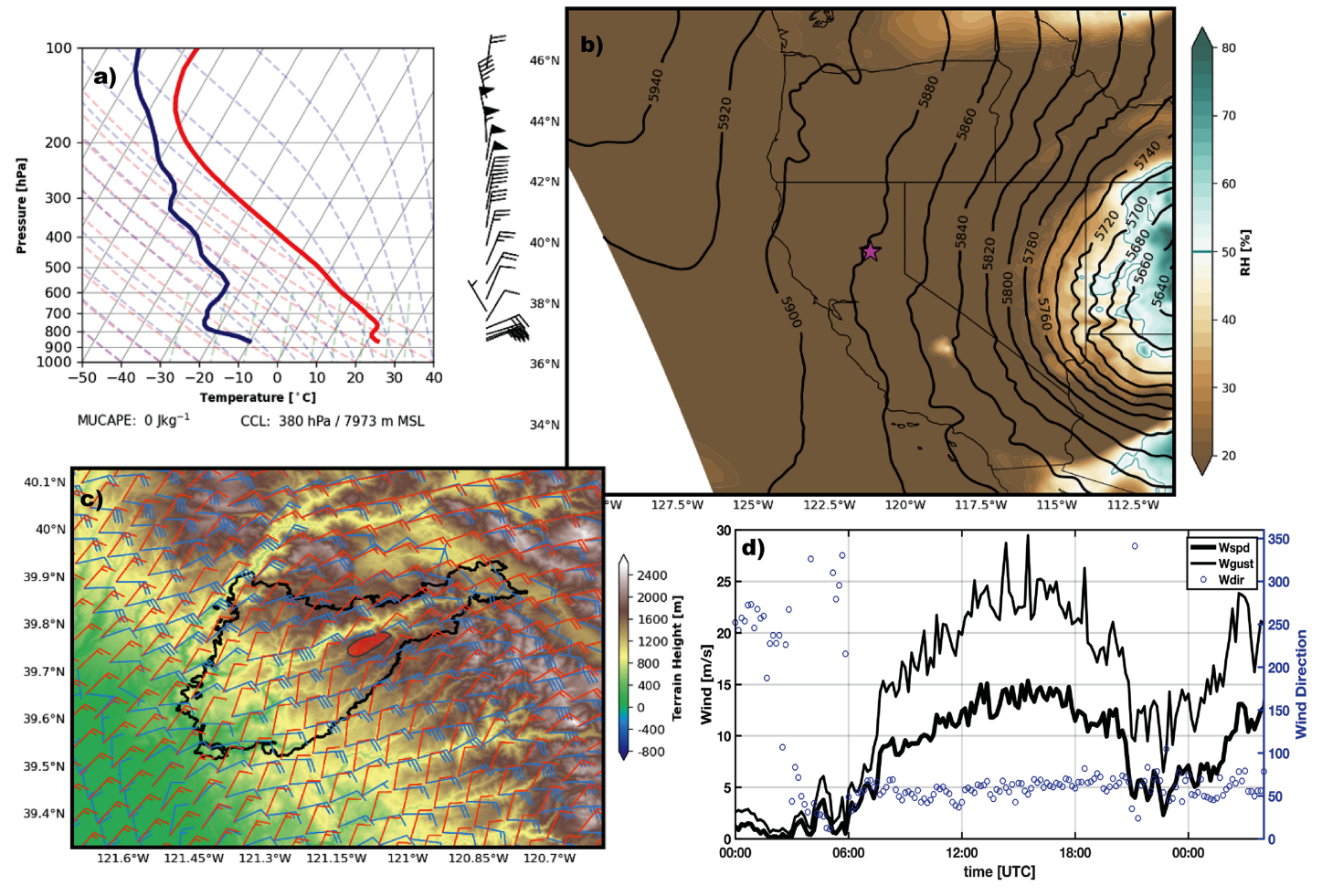


Fig. 9. Overview of the meteorology during the Bear Fire on 9 Sep 2020. (a) HRRR model sounding; (b) 500-hPa heights (in m) and 700–400-hPa layer-averaged relative humidity (shading); (c) wind barbs for the surface (blue) and 700 hPa (red) along with the fire perimeters (black line), approximate vortex zone (red shaded), and topography (terrain shaded); and (d) time series of wind speed and direction from a location just north of the Bear Fire.

~4.2 m s⁻¹. A third vortex was also apparent, but persisted for only ~2 min. This evolution indicates these are *shedding* vortices similar to those during the later stages of the Loyalton Fire (cf. with the magenta triangles in Figs. 5a,b). As with the Loyalton Fire these vortices may carry embers and flaming gases, leading to accelerated fire spread through this region.

The accompanying radar volume and vortex-line renderings show that the vortices diminish in depth as they move downstream and detach from the left flank of the head fire (i.e., moving right to left in the image; Figs. 11g,h). The vortices also occur downwind from where the flanking plume merges with the head fire's updraft and lifts from its near-surface trajectory (annotation arrows in Figs. 11g,h), which is consistent with the location of wake-like vortices found in laboratory experiments (e.g., Fric and Roshko 1994). The accompanying webcam snapshot shows the approximate location of these FGTVs, though the vortices are cloaked in smoke and ash (Fig. 11i).

Both the volumetric and near-surface reflectivity data also indicate counterclockwise curvature in the ash fall region extending away from the head fire (Figs. 11a,g,h). As with the previous cases, this curvature is indicative of the backing winds, which turn from northeast near the surface to northerly aloft (as shown in Figs. 9a,c). This is also apparent in the photograph, which shows dense smoke and ash spreading southward above the vortex zone.

In summary, the Bear Fire provides an interesting case of strong, near-surface winds and strong, but transient, FGTVs that propagate away from the head fire along an anticyclonic

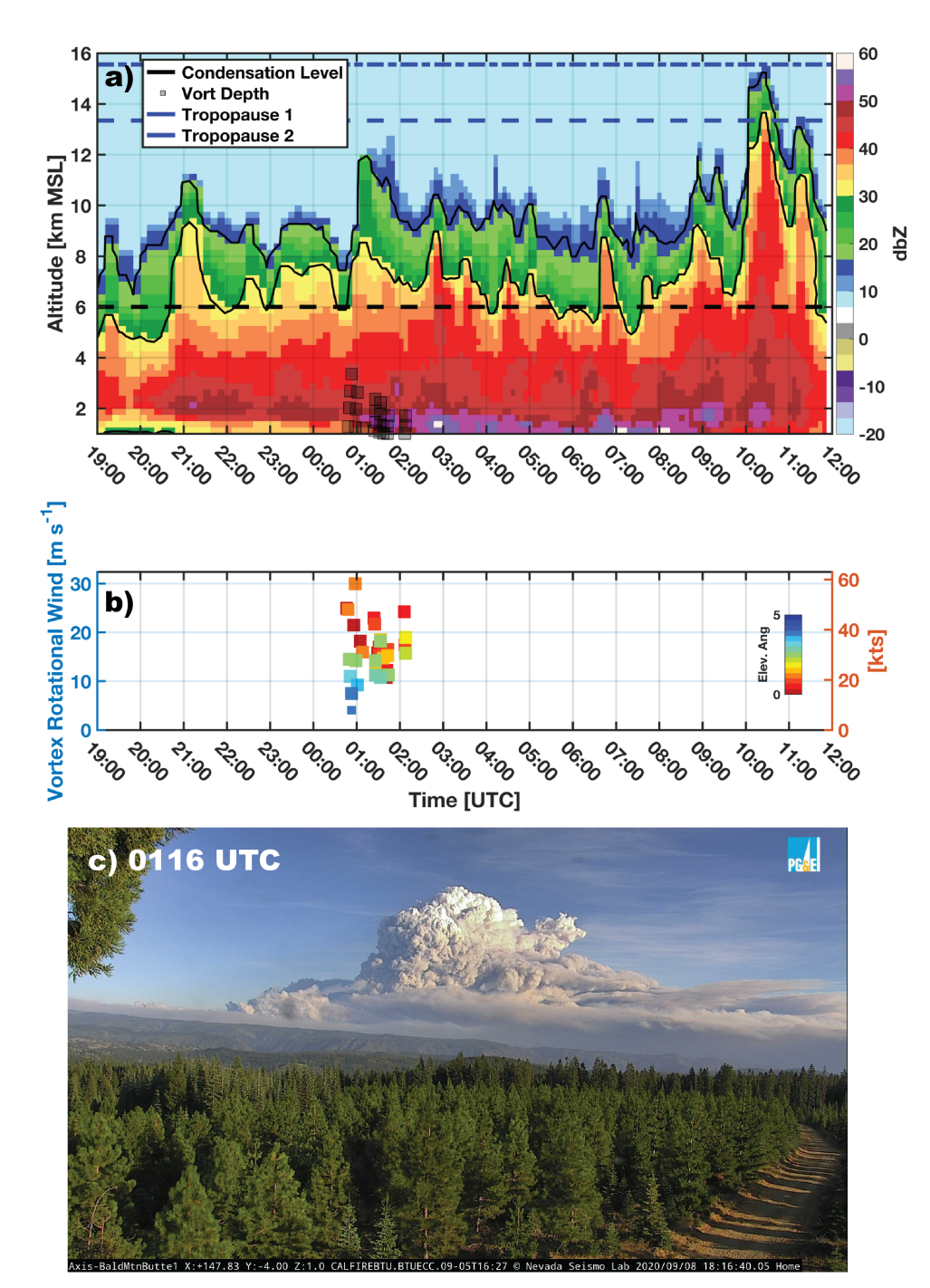


Fig. 10. Overview of the Bear Fire's plume growth and FGTV generation. (a) Radar reflectivity time-height diagram showing the plume tops (black line), estimated CCL (black dashed line), tropopause heights (dashed blue lines, note double tropopause), and the vortex vertical extents (black squares). (b) Time series of the rotation velocity (m s⁻¹ on left axis, kt on right axis) for different radar elevation scans (colors). The black dashed lines indicates the 20 m s⁻¹ line, which is linked to intense vortices. (c) Photograph of the Bear Fire pyroCu/Cb.

shear zone. Thus, there are similarities to the subset of shedding vortices observed during the Loyalton Fire and to the broader disruption of the flow apparent in all three cases. These similarities set the stage for the following synthesis of these FGTV events.

COMMON RADAR SIGNATURES. Commonalities among the Loyalton, Creek, and Bear Fires provide the building blocks for a FGTV conceptual model. These common features, summarized schematically in Fig. 12, are as follows:

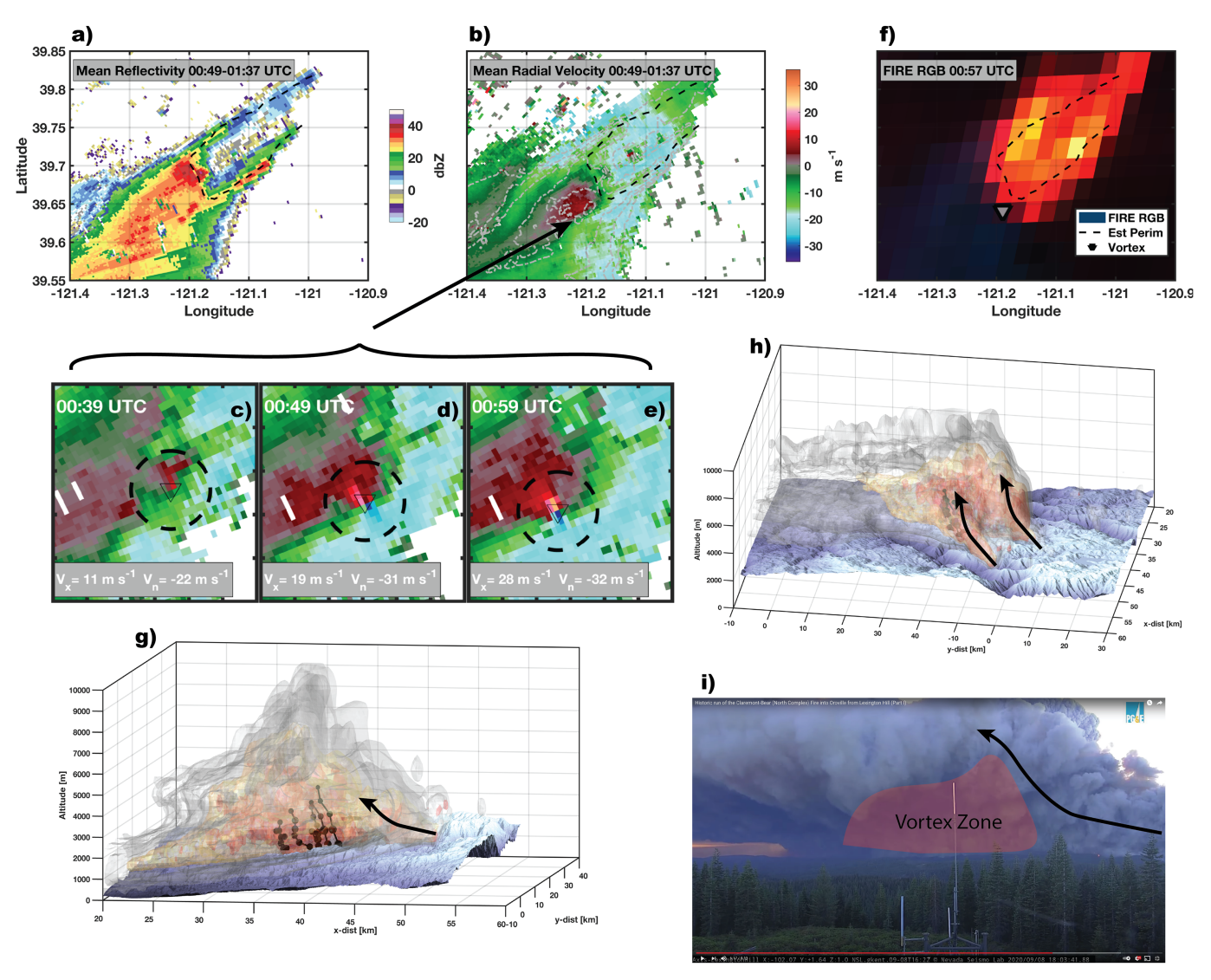


Fig. 11. Overview of intense FGTVs during Bear Fire. (a) Radar reflectivity and (b) radial velocity averaged for 0049–0137 UTC. (c)–(e) The fire perimeter is approximated (black dashed line) and the most intense FGTV signature is shown in the insets. The green and red colors are flow toward and away from the radar, respectively. (f) Fire–RGB satellite imagery showing the fire location and relative intensity along with estimated fire perimeters and FGTV locations. (g),(h) Radar reflectivity isosurfaces of the time-averaged plume structure from the (g) south and (h) east. The solid black lines and filled circles indicate vortex lines, with the marker size scaled to the rotational velocity. (i) Webcam still (from AlertWidfire/Nevada Seismological Laboratory) at 0103 UTC showing the flow features and approximate vortex locations.

- 1) Anticyclonic vortices (triangles) with rotational velocity exceeding 20 m s⁻¹ (40 kt) on the left flank of the asymmetric head fire (black oval in top panels) with two distinct morphologies:
 - (i) *Embedded FGTVs* within the high-reflectivity updraft cores and anchored to the fire (red triangles).
 - (ii) *Shedding FGTVs* moving away from the fire along the periphery of the reversed flow (magenta triangles) and pendant from the bent-over plume.
- 2) Flow splitting (blue arrows) and flow reversal (red arrows) around the head fire indicative of CVPs (blue and red circles). The flow reversal can extend >10 km downwind from the fire
- 3) Counterclockwise curving ashfall extending downwind from the head fire indicative of a backing wind profile (see inset wind barbs).
- 4) Bent-over and bifurcating plume structures associated with the CVP (as shown in earlier volume renderings, e.g., Fig. 5d).

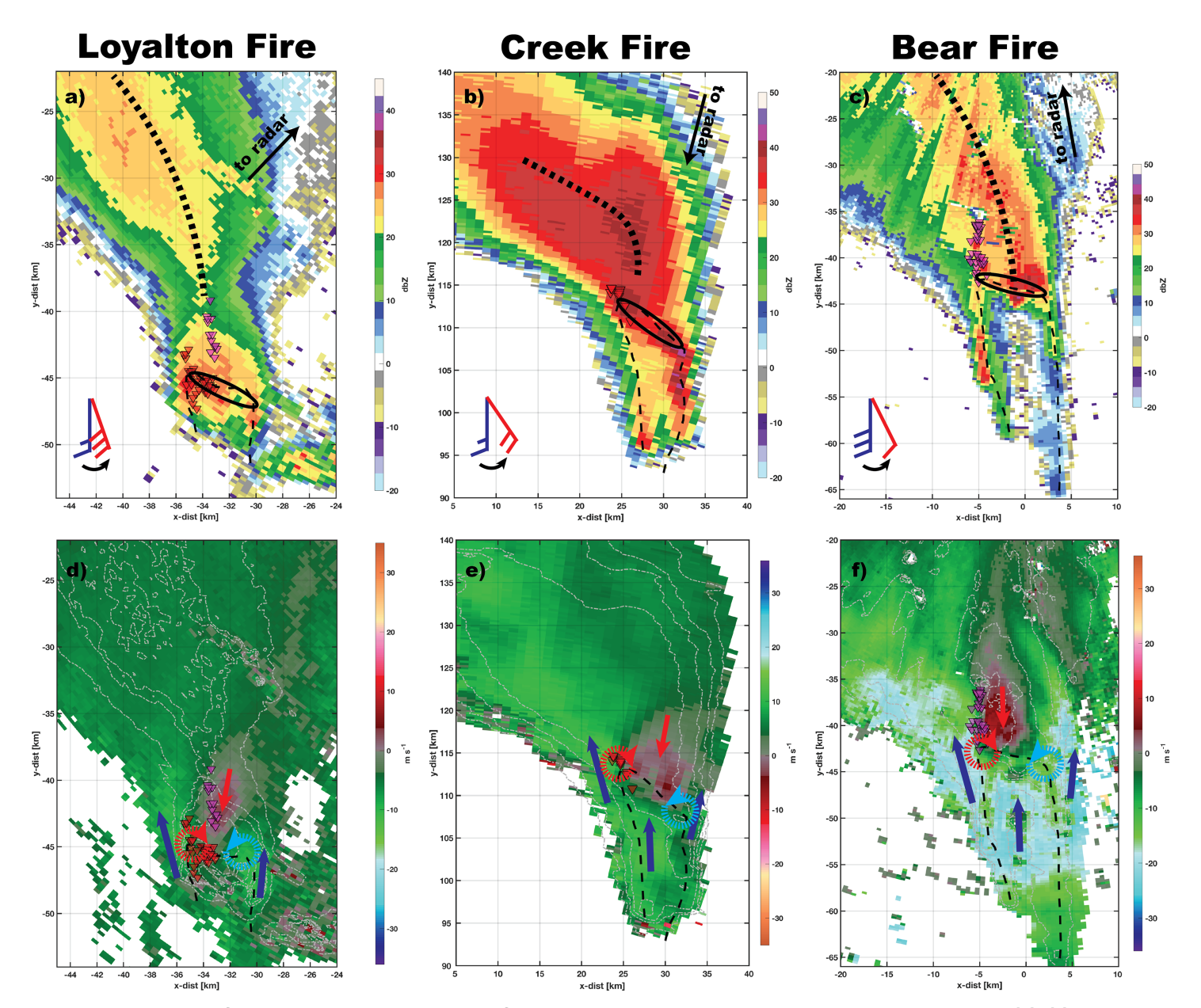


Fig. 12. Overview of the time-averaged radar reflectivity and radial velocity during our three cases. (a)–(c) The time-averaged reflectivity annotated to indicate the orientation of the head fire (black oval), approximate fire perimeter (narrow black dashed line), and curvature of the ash-fall region (thick black dashed line). Wind barbs show the near surface (blue) and midtropospheric (red) wind speed and direction, noting that the axes have been rotated to facilitate comparison. (d)–(f) The time-averaged radial velocity component with annotations showing flow splitting and enhancement (blue arrows), flow reversal downstream of the head fire (red arrows), and the location of the mean-state counter-rotating vortex pair (red = anticyclonic, blue = cyclonic). Note that the color bar is reversed for the Creek Fire to facilitate the comparison (i.e., the green flows are outbound).

5) Deepening pyroconvection, including pyroCb, with plume tops reaching 12+ km MSL during FGTV periods (as shown in earlier time—height diagrams).

Many of these common features are strikingly similar to those observed in laboratory experiments with jets, plumes, and flames in cross flow (cf. Fig. 1; Fric and Roshko 1994; Wu et al. 1988; Shinohara and Matsushima 2012), and consistent with descriptions of FGVs in Countryman (1971) and other reviews (Cunningham et al. 2005; Forthofer and Goodrick 2011; Potter 2012; Tohidi et al. 2018). To be specific, observations and experiments both indicate steady-state CVPs, flow splitting and reversal, and wake-like vortices pendant from the plume (in the case of the Loyalton and Bear Fires). We note that our embedded vortices

are consistent with the hypothesis of Shinohara and Matsushima (2012) that CVPs could be responsible for large FGVs in landscape scale fires, and our shedding vortices are consistent with the "tornado-like" wake vortices described in Fric and Roshko (1994). Our embedded and shedding vortex morphologies are also broadly consistent with *quasi-steady on-source* and *unsteady off-source* whirls, respectively, discussed in Tohidi et al. (2018), wherein the source refers to the fuel bed.

While laboratory studies provide intriguing analogs to our FGTV cases, it is important to acknowledge that these real-world scenarios include additional complexities. These include, but are not limited to, 1) the influence of stratification, apparent as the descending branch of the plumes; 2) the contribution of latent heating in the pyroCb to the plume structure and kinematics; 3) ambient turbulence in the convective boundary layer; 4) unsteadiness in the combustion; and 5) a host of terrain-flow effects, some of which are discussed below. Future work will need to isolate the importance of these processes.

An additional complexity in our cases is the tendency for fire—flow interactions to favor FGTVs on one flank of the fire, in this case, the anticyclonic flank. This may provide important context for identifying when and where a fire will yield an FGTV. We note that the angled head fire structures in our cases are similar to that of oval jets inclined to the cross flow, which produce asymmetric vortex structures in laboratory experiments (Wu et al. 1988). Fire-geometry and cross-flow interactions have also been linked to vortex generation in other laboratory and wildfire studies (e.g., Kuwana et al. 2013; Peace et al. 2015). It is also possible that backing wind profiles favor anticyclonic vortices via linear dynamic pressure perturbations akin to those in mesocyclonic thunderstorms forming in sheared environments (Markowski and Richardson 2011). Indeed, simulations of buoyant plumes from hydrothermal vents in sheared flows (i.e., Ekman layer) also generate asymmetric CVPs (Lavelle 1997).

To this end, observations from other fires suggest a possible sensitivity to the wind profile. For example, Fig. 13 shows radar observations of two other pyroCb plumes (King and Apple Fires; see Table 1) that produced CVPs with flow splitting and flow reversal (arrow annotations in Fig. 13), but did not produce FGTVs. Notably, these cases have only speed shear, evident in the ash fall extending in a straight, rather than curved, trajectory from the head fire (black dashed line). They also have weaker flow reversal, which may be indicative of plumes less conducive to FGTV development due to less disruption of the cross flow. This may be analogous to identifying difference between nontornadic and tornadic supercells where environmental factors (shear, moisture, etc.) modulate the potential for tornadoes or in our cases, FGTVs. Future idealized modeling studies should be conducted to explore these shear-plume interactions and sensitivities, which may yield a better understanding of what tips the balance between the common CVP signature and rare FGTV formation.

FGTVs in context. It is important to place FGTV strength ($V_{\rm rot}$), depth, and damage in the context of ordinary tornadoes (Fig. 14). This is accomplished using a database of tornado $V_{\rm rot}$, debris signature (TDS) heights, and "enhanced Fujita scale" (EF) damage ratings (www.spc. noaa.gov/efscale/ef-scale.html; Emmerson et al. 2019, 2020). For the FGTVs we use the estimated vortex top rather than TDS (see supplemental material text), which is not defined for FGTVs, and limit the analysis to the strongest and deepest FGTVs. These comparisons indicate that the FGTVs during the Creek and Loyalton Fires are consistent with observations of EF2-3 strength tornadoes. The Bear Fire FGTV, which was strong but shallow, resides within the considerable overlap among EF1-3 strength tornadoes. These EF ranges are consistent with the conditional probabilities provided by Smith et al. (2020), who show that $V_{\rm rot}$ of 60-69.9 kt, as observed in the Creek Fire, yields 98%, 60%, and 23% probabilities of exceeding EF1, EF2, and EF3 damage, respectively (see Fig. 7 in Smith et al. 2020). We note that the Carr Fire FGTV, documented in Lareau et al. (2018), has not been included in Fig. 14 because

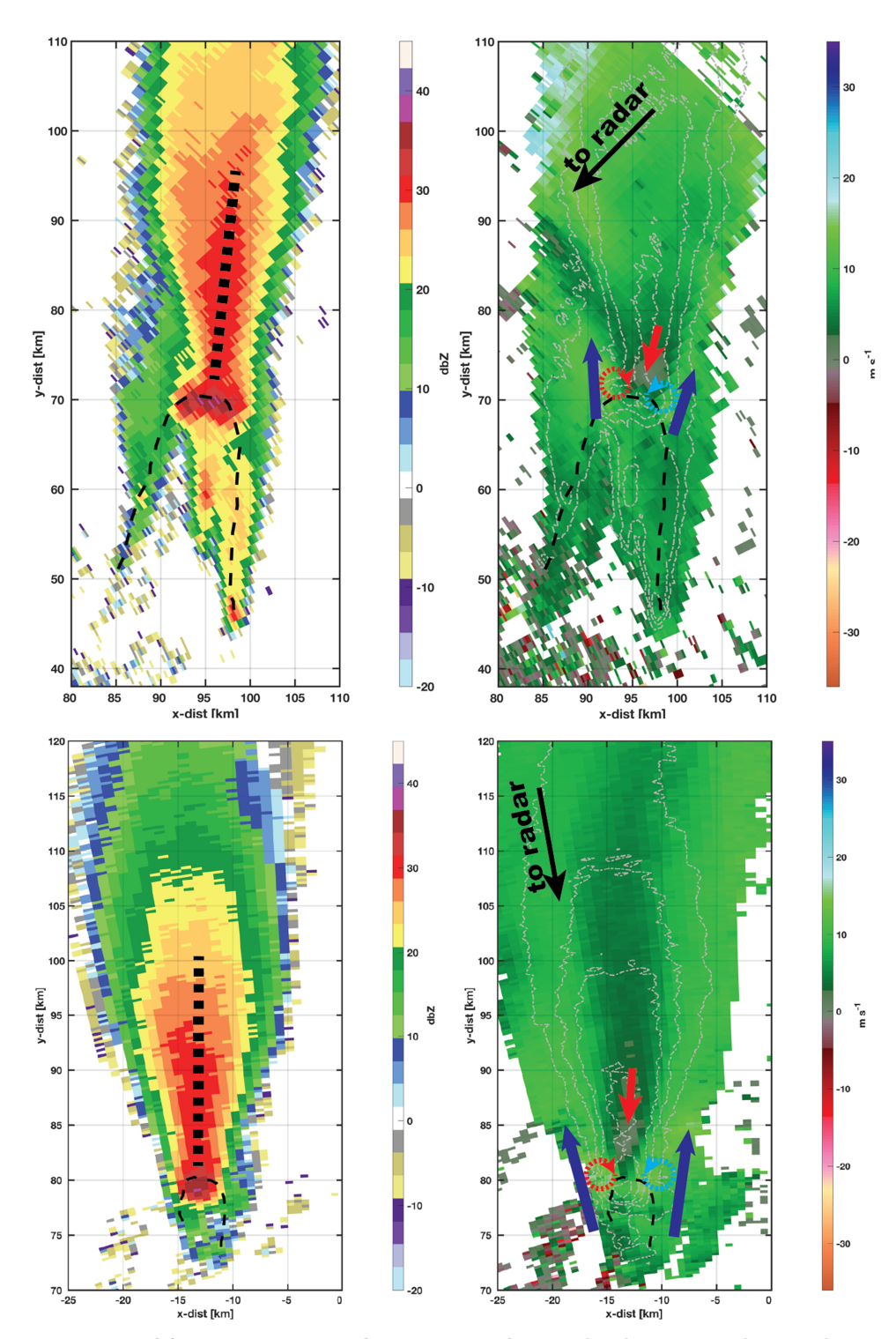


Fig. 13. Examples of flow splitting and flow reversal for the (top) King and (bottom) Apple Fires. Annotations are as in Fig. 11.

the radar beam height was very high above the surface (~3.5 km, ~11,500 ft), such that the documented $V_{\rm rot}$ of ~17.5 m s⁻¹ (34 kt) and vortex depth (~4.5 km, ~15,000 ft) would not make sense in the context of these other data. That said, the Carr Fire's FGTV depth was comparable to that of the Creek Fire and Loyalton Fires, and interpreted in the context of these other data points is consistent with its EF3 rating and estimated surface winds of >60 m s⁻¹.

FGTV damage during the Loyalton and Creek Fires was confirmed by National Weather Service (NWS) meteorologists. For the Loyalton Fire, a damage survey found sheared off and uprooted large-diameter trees consistent with EF1 damage, though we note that available damage indicators were sparse (www.ncdc.noaa.gov/stormevents/eventdetails.jsp?id=916709).

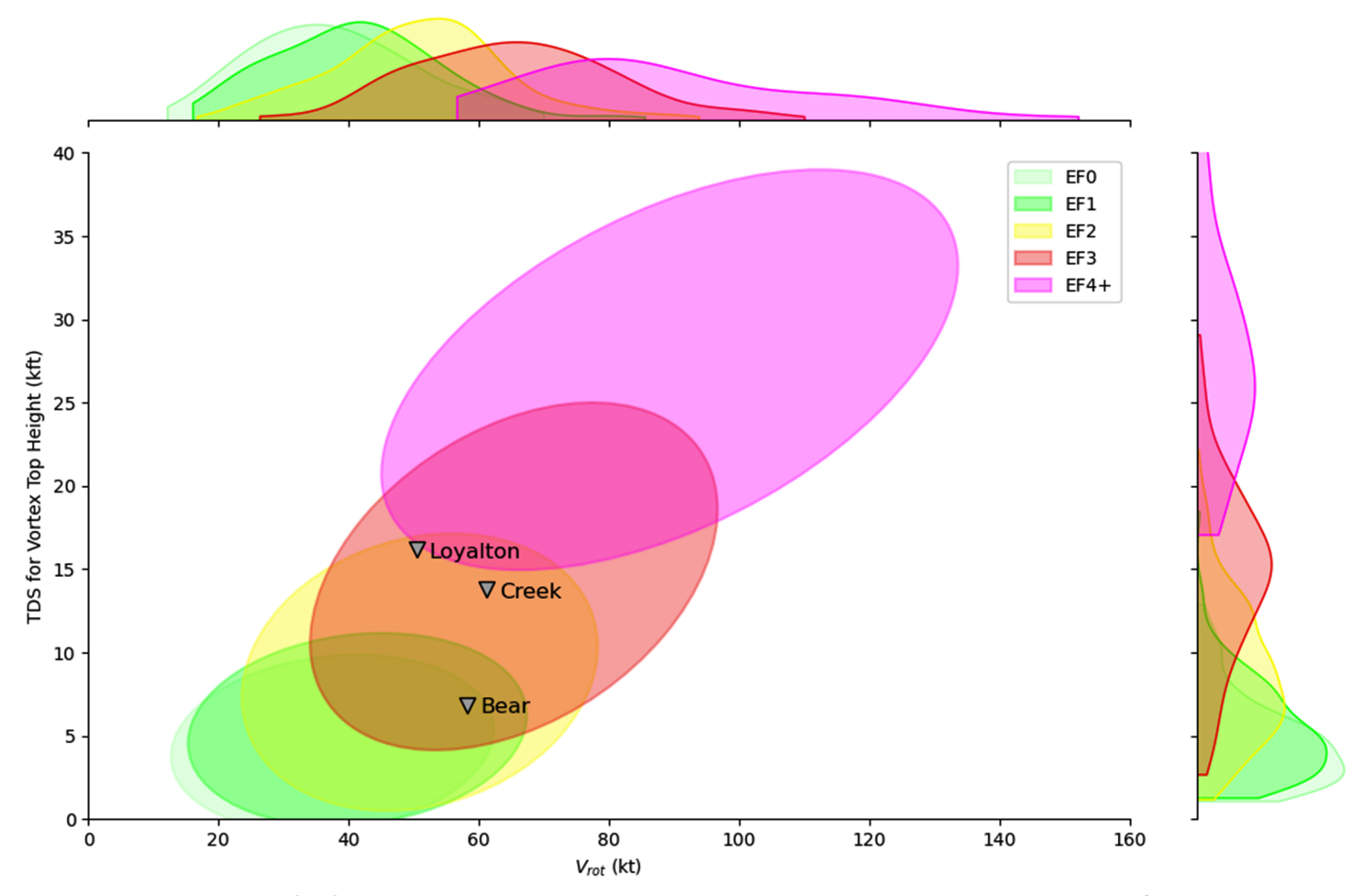


Fig. 14. FGTV strength (V_{rot}) and depth observations contextualized with the probability density function and joint probability density functions for V_{rot} and tornado debris signature (TDS) heights derived from a large sample of ordinary tornadoes. The ellipses correspond to two standard deviations (~95% confidence) within the V_{rot} -TDS height parameter space for each EF-scale category.

For the Creek Fire, an Incident Meteorologist (IMET) documented EF2 damage in a location consistent with the peak radar observed winds (see Fig. 8e). Damage included multiple 2-ft-diameter trees snapped 20–30 ft up with branches and bark removed (www.ncdc.noaa.gov/stormevents/eventdetails.jsp?id=921844; 1 ft \approx 0.305 m)

The radar estimated and observed impacts of FGTVs underscore their threat and the need to warn for their development, as was done with the first-ever NWS tornado warning for the Loyalton Fire's FGTVs. Future dialogue among wildfire stakeholders and weather forecasters will be needed to establish and refine warning criteria for these events.

Site specific factors Influencing FGTVs. Site-specific factors, including terrain, fuels, and microto mesoscale flows can impact FGTV development. It is known, for example, that lee sides of ridges can generate flows conducive to vortices (Simpson et al. 2013; Sharples and Hilton 2020), as can the arrangement of fuel loads (Zhou and Wu 2007). To examine these factors, Fig. 15 shows the terrain (hill shaded) and satellite imagery, representing the prefire fuel distributions, for each fire. The Loyalton Fire FGTVs occurred over a 10-km span on lee slopes (in southwest winds) and moved from heavier fuels at upper elevations to lighter, flashier fuels (Table 2) at lower elevations. The Creek Fire FGTVs occurred along a >10-km span along the west edges of the deeply incised San Joaquin River valley, and then into higher-elevation terrain. The fuels ranged from brush and grasses to heavy timber (Table 2). The Bear Fire's FGTVs occurred along a plateau, moving through a patchwork of previously logged plots. While informative, these limited observations are insufficient

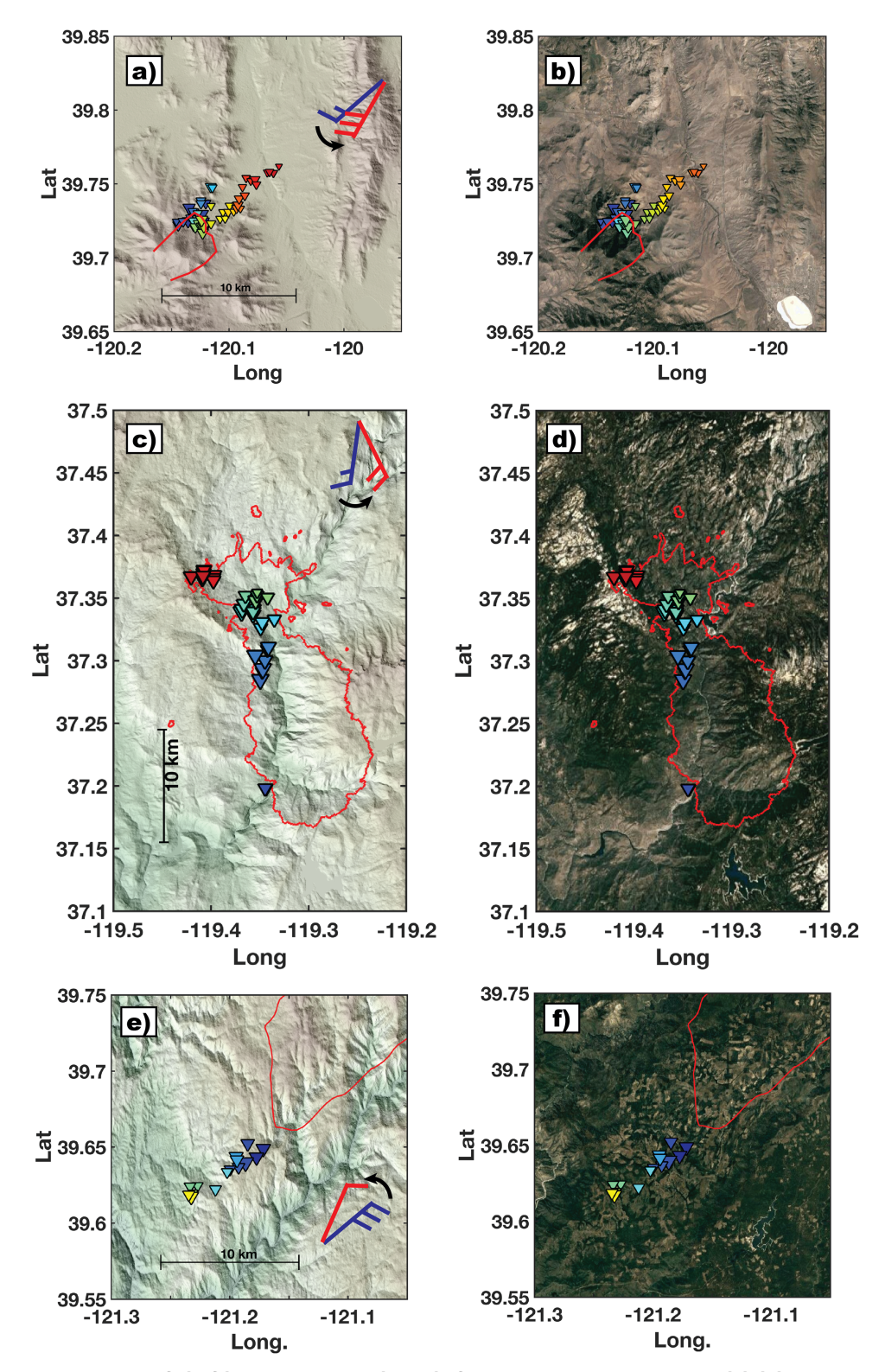


Fig. 15. Overview of (left) terrain and (right) fuels during the FGTVs: (a),(b) Loyalton Fire, (c),(d) Creek Fire, (e),(f) Bear Fire. In each panel the vortex locations are shown as triangles, with color fill indicating relative time (blue is earlier, red is later), and marker size indicating vortex strength. Also shown are the fire perimeters (red lines), which are estimated for the Loyalton and Bear Fires, and from NIROPs for the Creek Fire at ~0600 UTC 6 Sep 2020. A scale bar, showing 10 km, is included, as are the approximate surface (blue) and midtropospheric (red) wind barbs.

to establish the importance of terrain and fuels on FGTV development. That said, we believe the commonalities in plume and vortex structures among our cases suggest that terrain and fuels are not the dominant factor in these FGTVs. For example, the Creek Fire

generated FGTVs over a span of 9 h as the fire progressed ~20 km, moving through varying terrain and fuel loads. Clearly then, no one specific terrain feature or fuel configuration could explain the persistent FGTVs, which remained in a fixed location relative to the fire and plume.

Summary

We have presented three cases of large, high-impact wildfires in California that produced fire-generated tornado-strength vortices (FGTVs) and pyroCb. Using radar and satellite observations we documented FGTV strengths, depths, and locations and placed those data in the broader context of the wildfire plume structure and fire evolution. The observations indicate long-lived anticyclonic vortices with rotational velocity up to 30 m s $^{-1}$ (60 kt), vortex depths as great as 4.9 km AGL, and plume tops as high as 16 km MSL.

From these observations we have identified two distinct FGTV morphologies: 1) *embedded* vortices residing within one branch of the counter rotating vortex pair and anchored to the fire, and 2) *shedding* vortices, which detach from the fire and progress downstream while pendant from the bent-over plume. In addition, we have documented common flow and plume features linked to the FGTVs, which include prominent mesoscale flow reversal downstream of the head fire, flow splitting around the fire's updraft, and bent-over plume structures due to the interaction of the plumes with the crosswind. We have also shown that the vortex cores, in two cases, reach pyroCb cloud base and that vortex strength covaries with pyroCb plume depth, suggesting two-way links between the cloud processes aloft and the vortex processes at the surface.

The inferences from this study compliment the understanding gained from previous FTGV cases, including the Carr Fire in Redding, California, United States (Lareau et al. 2018), and the 2003 Black Saturday Fires in Canberra, Australia (Fromm et al. 2006; McRae et al. 2013). These new observations help contextualize these previous events, confirming the link to rapidly deepening pyroCb, but now adding important dynamical insights that better explain where in a fire FGTVs form.

To better understand complexities of FGTV development, including the links to pyroCb, future research with coupled fire—atmosphere models, idealized simulations, and high-resolution observations are needed. Peace et al. (2015), for example, show that the Weather and Forecasting (WRF) Model coupled with a fire-spread model (SFIRE) can produce FGVs, but only when two-way coupling between the fire and atmosphere are used. Idealized large-eddy simulations can also provide insight into the sensitivities of FGTV and pyroconvective development to wind shear, moisture, and fire geometry (e.g., Cunningham and Reeder 2009; Badlan et al. 2021a,b). Finally, and perhaps most importantly, observations with scanning radars and lidars capable of resolving the process-level details of FGVs and FGTVs are needed (e.g., Clements et al. 2018; Aydell and Clements 2021). Such data will help establish the formative mechanisms for, and kinematic structure of, FGV and FGTVs, and may help us distinguish between fires that do and do not produce FGTVs.

Finally, while FGTVs remain rare, the occurrence of four (three reported here, one in Lareau et al. 2018) in the past 2 years alone suggests that emergent trends in fire intensity (Williams et al. 2019; Abram et al. 2021) may yield increasing FGTV occurrence. In fact, in the time since the inception of this manuscript, initial reports suggest at least one deadly FGTV formed during the 2019/20 pyroCb super-outbreak in Australia (www.theguardian.com/australia-news/2019/dec/31/volunteer-firefighter-samuel-mcpaul-died-when-fire-tornado-overturned-10-tonne-truck; Peterson et al. 2021), and early evidence from the Bootleg Fire during July 2021 in Oregon, United States, indicate a likely FGTV (www.heraldandnews.com/news/local_news/bootleg-fire-formed-a-tornado-with-wind-speeds-higher-than-111-mph/article_0a4c466d-0a77-5b09-9411-fd04f2723251.html). Considering these events and noting that climate projections indicate

conditions increasingly conducive to extreme pyroconvection (Dowdy et al. 2019), there is a continuing need to advance our understanding of, and ability to warn for, fire-generated extreme weather including FGTVs.

Acknowledgments. Funding for this work is provided, in part, by the National Science Foundation under Grants AGS-2114251 and CMMI-1953333. Additional support was provided by the National Interagency Fire Center (NIFC) and the Storm Prediction Center. We thank Dr. David Peterson and two anonymous reviewers for their constructive critiques that improved this manuscript. We thank Drs. Mika Peace, Kevin Tory, Barry Hanstrum, and Jeff Kepert of Australia's Bureau of Meteorology for their comments and suggestions. We thank the AlertWildfire camera network, the Nevada Seismological Laboratory, CalFire, and Pacific Gas and Electric (PG&E) for webcam footage and still images of wildfires. We thank Jordan Hewlett, Alex Neigher, and Thalia Dockery for use of photographs.

Data availability statement. NEXRAD and *GOES-17* data can be obtained from the Amazon cloud at https://registry.opendata.aws/noaa-nexrad/ and https://registry.opendata.aws/noaa-goes/. HRRR data can be accessed via the University of Utah archive (doi: 10.7278/S5JQ0Z5B) courtesy of Brian Blaylock. Fire perimeter data are available at https://ftp.wildfire.gov/.

References

- Abram, N. J., and Coauthors, 2021: Connections of climate change and variability to large and extreme forest fires in southeast Australia. *Commun. Earth Environ.*, **2**, 8, https://doi.org/10.1038/s43247-020-00065-8.
- Aydell, T. B., and C. B. Clements, 2021: Mobile Ka-band polarimetric Doppler radar observations of wildfire smoke plumes. *Mon. Wea. Rev.*, **149**, 1247–1264, https://doi.org/10.1175/MWR-D-20-0198.1.
- Badlan, R. L., J. J. Sharples, J. P. Evans, and R. H. D. McRae, 2021a: Factors influencing the development of violent pyroconvection. Part I: Fire size and stability. *Int. J. Wildland Fire*, 30, 484–497, https://doi.org/10.1071/WF20040.
- ——, J. J. Sharples, J. P. Evans, and R. H. D. McRae, 2021b: Factors influencing the development of violent pyroconvection. Part II: Fire geometry and intensity. *Int. J. Wildland Fire*, 30, 498–512, https://doi.org/10.1071/WF20041.
- Banta, R. M., L. D. Olivier, E. T. Holloway, R. A. Kropfli, B. W. Bartram, R. E. Cupp, and M. J. Post, 1992: Smoke-column observations from two forest fires using Doppler lidar and Doppler radar. *J. Appl. Meteor. Climatol.*, 31, 1328–1349, https://doi.org/10.1175/1520-0450(1992)031<1328:SCOFTF>2.0.CO;2.
- Benjamin, S. G., and Coauthors, 2016: A North American hourly assimilation and model forecast cycle: The Rapid Refresh. *Mon. Wea. Rev.*, 144, 1669–1694, https://doi.org/10.1175/MWR-D-15-0242.1.
- Cappucci, M., 2020: A freak fire tornado warning was issued in California on Saturday amid swarm of spinning blazes. Washington Post, 16 August, www. washingtonpost.com/weather/2020/08/16/california-fire-tornado-warning/.
- Church, C. R., J. T. Snow, and J. Dessens, 1980: Intense atmospheric vortices associated with a 1000 MW fire. *Bull. Amer. Meteor. Soc.*, 61, 682–694, https://doi.org/10.1175/1520-0477(1980)061
- Clark, T. L., M. A. Jenkins, J. L. Coen, and D. R. Packham, 1996: A coupled atmospherefire model: Role of the convective Froude number and dynamic fingering at the fireline. *Int. J. Wildland Fire*, 6, 177–190, https://doi.org/10.1071/WF9960177.
- Clements, C. B., N. P. Lareau, D. E. Kingsmill, C. L. Bowers, C. P. Camacho, R. Bagley, and B. Davis, 2018: The Rapid Deployments to Wildfires Experiment (RaDFIRE): Observations from the fire zone. *Bull. Amer. Meteor. Soc.*, 99, 2539–2559, https://doi.org/10.1175/BAMS-D-17-0230.1.
- Countryman, C. M., 1971: Fire whirls...why, when, and where. USDA Forest Service, Pacific Southwest Forest and Range Experiment Station, 14 pp.
- Cunningham, P., and M. J. Reeder, 2009: Severe convective storms initiated by intense wildfires: Numerical simulations of pyro-convection and pyro-tornadogenesis. *Geophys. Res. Lett.*, **36**, L12812, https://doi.org/10.1029/2009GL039262.
- ——, S. L. Goodrick, M. Y. Hussaini, and R. R. Linn, 2005: Coherent vortical structures in numerical simulations of buoyant plumes from wildland fires. *Int. J. Wildland Fire*, **14**, 61–75, https://doi.org/10.1071/WF04044.
- Dowdy, A. J., H. Ye, A. Pepler, M. Thatcher, S. L. Osbrough, J. P. Evans, G. Di Virgilio, and N. McCarthy, 2019: Future changes in extreme weather and pyroconvection risk factors for Australian wildfires. *Sci. Rep.*, 9, 10073, https://doi. org/10.1038/s41598-019-46362-x.
- Emmerson, S. W., S. E. Nelson, and A. K. Baker, 2019: A comprehensive analysis of tornadic debris signatures associated with significant tornadoes from 2010– 2017. 18th Annual Student Conf., Phoenix, AZ, Amer. Meteor. Soc., S210, https://ams.confex.com/ams/2019Annual/webprogram/Paper356019.html.
- ——, S. E. Nelson, and R. L. Thompson, 2020: Using characteristics of tornadic debris signatures to estimate tornado intensity. 30th Conf. on Weather Analysis and Forecasting/26th Conf. on Numerical Weather Prediction, Boston, MA, Amer. Meteor. Soc., 8B.5, https://ams.confex.com/ams/2020Annual/webprogram/Paper368640.html.
- Forthofer, J. M., and S. L. Goodrick, 2011: Review of vortices in wildland fire. *J. Combust.*, **2011**, 984363.
- Fric, T. F., and A. Roshko, 1994: Vortical structure in the wake of a transverse jet. *J. Fluid Mech.*, **279**, 1–47, https://doi.org/10.1017/S0022112094003800.
- Fromm, M., A. Tupper, D. Rosenfeld, R. Servranckx, and R. McRae, 2006: Violent pyroconvective storm devastates Australia's capital and pollutes the stratosphere. *Geophys. Res. Lett.*, **33**, L05815, https://doi.org/10.1029/2005GL025161.

- ——, D. T. Lindsey, R. Servranckx, G. Yue, T. Trickl, R. Sica, P. Doucet, and S. Godin-Beekmann, 2010: The untold story of pyrocumulonimbus. *Bull. Amer. Meteor. Soc.*, **91**, 1193–1210, https://doi.org/10.1175/2010BAMS3004.1.
- Gibbs, J. G., 2016: A skill assessment of techniques for real-time diagnosis and short-term prediction of tornado intensity using the WSR-88D. J. Operat. Meteorol., 4, 170–181, https://doi.org/10.15191/nwajom.2016.0413.
- Haines, D. A., and M. C. Smith, 1987: Three types of horizontal vortices observed in wildland mass and crown fires. J. Appl. Meteor. Climatol., 26, 1624–1637, https://doi.org/10.1175/1520-0450(1987)026<1624:TTOHVO>2.0.CO;2.
- Hissong, J. E., 1926: Whirlwinds at oil-tank fire, San Luis Obispo, Calif. *Mon. Wea. Rev.*, **54**, 161–163, https://doi.org/10.1175/1520-0493(1926)54<161:WAOF SL>2 0 CO:2
- Kuwana, K., K. Sekimoto, T. Minami, T. Tashiro, and K. Saito, 2013: Scale-model experiments of moving fire whirl over a line fire. *Proc. Combust. Inst.*, 34, 2625–2631, https://doi.org/10.1016/j.proci.2012.06.092.
- Lareau, N. P., and C. B. Clements, 2016: Environmental controls on pyrocumulus and pyrocumulonimbus initiation and development. *Atmos. Chem. Phys.*, 16, 4005–4022, https://doi.org/10.5194/acp-16-4005-2016.
- ——, N. J. Nauslar, and J. T. Abatzoglou, 2018: The Carr Fire vortex: A case of pyrotornadogenesis? *Geophys. Res. Lett.*, 45, 13107–13115, https://doi.org/10.1029/2018GL080667.
- LaRoche, K. T., and T. J. Lang, 2017: Observations of ash, ice, and lightning within pyrocumulus clouds using polarimetric NEXRAD radars and the national lightning detection network. *Mon. Wea. Rev.*, **145**, 4899–4910, https://doi. org/10.1175/MWR-D-17-0253.1.
- Lavelle, J. W., 1997: Buoyancy-driven plumes in rotating, stratified cross flows: Plume dependence on rotation, turbulent mixing, and cross-flow strength. J. Geophys. Res., 102, 3405–3420, https://doi.org/10.1029/96JC03601.
- Luderer, G., J. Trentmann, T. Winterrath, C. Textor, M. Herzog, H. F. Graf, and M. O. Andreae, 2006: Modeling of biomass smoke injection into the lower stratosphere by a large forest fire (Part II): Sensitivity studies. *Atmos. Chem. Phys.*, 6, 5261–5277, https://doi.org/10.5194/acp-6-5261-2006.
- ——, and M. O. Andreae, 2009: A new look at the role of fire-released moisture on the dynamics of atmospheric pyro-convection. *Int. J. Wildland Fire*, **18**, 554–562, https://doi.org/10.1071/WF07035.
- Mahesh, K., 2013: The interaction of jets with crossflow. *Annu. Rev. Fluid Mech.*, **45**, 379–407, https://doi.org/10.1146/annurev-fluid-120710-101115.
- Markowski, P., and Y. Richardson, 2011: *Mesoscale Meteorology in Midlatitudes*. Vol. 2. John Wiley & Sons, 432 pp.
- McCarthy, N., A. Guyot, A. Dowdy, and H. McGowan, 2019: Wildfire and weather radar: A review. J. Geophys. Res. Atmos., 124, 266–286, https://doi.org/10.1029/2018JD029285.
- McRae, R. H., J. J. Sharples, S. R. Wilkes, and A. Walker, 2013: An Australian pyrotornadogenesis event. *Nat. Hazards*, **65**, 1801–1811, https://doi.org/10.1007/s11069-012-0443-7.
- Peace, M., T. Mattner, G. Mills, J. D. Kepert, and L. McCaw, 2015: Fire-modified meteorology in a coupled fire—atmosphere model. *J. Appl. Meteor. Climatol.*, 54, 704–720, https://doi.org/10.1175/JAMC-D-14-0063.1.
- ——, L. McCaw, B. Santos, J. D. Kepert, N. Burrows, and R. J. Fawcett, 2017: Meteorological drivers of extreme fire behaviour during the Waroona bushfire, Western Australia, January 2016. J. South. Hemisphere Earth Syst. Sci., 67, 79–106, https://doi.org/10.1071/ES17007.
- —, J. Charney, and J. Bally, 2020: Lessons learned from coupled fire-atmosphere research and implications for operational fire prediction and meteorological products provided by the Bureau of Meteorology to Australian Fire Agencies. Atmosphere, 11, 1380, https://doi.org/10.3390/atmos11121380.
- Peterson, D. A., E. J. Hyer, J. R. Campbell, M. D. Fromm, J. W. Hair, C. F. Butler, and M. A. Fenn, 2015: The 2013 Rim Fire: Implications for predicting extreme fire spread, pyroconvection, and smoke emissions. *Bull. Amer. Meteor. Soc.*, 96, 229–247, https://doi.org/10.1175/BAMS-D-14-00060.1.

- —, M. D. Fromm, J. E. Solbrig, E. J. Hyer, M. L. Surratt, and J. R. Campbell, 2017a: Detection and inventory of intense pyroconvection in western North America using *GOES-15* daytime infrared data. *J. Appl. Meteor. Climatol.*, **56**, 471–493, https://doi.org/10.1175/JAMC-D-16-0226.1.
- —, E. J. Hyer, J. R. Campbell, J. E. Solbrig, and M. D. Fromm, 2017b: A conceptual model for development of intense pyrocumulonimbus in Western North America. *Mon. Wea. Rev.*, 145, 2235–2255, https://doi.org/10.1175/MWR-D-16-0232.1.
- —, and Coauthors, 2021: Australia's Black Summer pyrocumulonimbus super outbreak reveals potential for increasingly extreme stratospheric smoke events. npj Climate Atmos. Sci. 4, 38, https://doi.org/10.1038/s41612-021-00192-9.
- Pirsko, A. R., L. M. Sergius, and C. W. Hickerson, 1965: Causes and behavior of a tornadic fire-whirlwind. Res. Note PSW-RN-061, U.S. Department of Agriculture, Forest Service, Pacific Southwest Forest and Range Experiment Station, 13 pp.
- Potter, B. E., 2012: Atmospheric interactions with wildland fire behaviour II. Plume and vortex dynamics. *Int. J. Wildland Fire*, **21**, 802–817, https://doi.org/10.1071/WF11129.
- Rodriguez, B., N. P. Lareau, D. E. Kingsmill, and C. B. Clements, 2020: Extreme pyroconvective updrafts during a megafire. *Geophys. Res. Lett.*, 47, e2020GL089001, https://doi.org/10.1029/2020GL089001.
- Sharples, J. J., and J. E. Hilton, 2020: Modeling vorticity-driven wildfire behavior using near-field techniques. Front. Mech. Eng., 5, 69, https://doi.org/10.3389/ fmech.2019.00069.
- Shinohara, M., and S. Matsushima, 2012: Formation of fire whirls: Experimental verification that a counter-rotating vortex pair is a possible origin of fire whirls. *Fire Saf. J.*, **54**, 144–153, https://doi.org/10.1016/j.firesaf.2012.03.009.
- Simpson, C. C., J. J. Sharples, J. P. Evans, and M. F. McCabe, 2013: Large eddy simulation of atypical wildland fire spread on leeward slopes. *Int. J. Wildland Fire*, 22, 599–614, https://doi.org/10.1071/WF12072.
- Smith, B. T., R. L. Thompson, D. A. Speheger, A. R. Dean, C. D. Karstens, and A. K. Anderson-Frey, 2020: WSR-88D tornado intensity estimates. Part I: Real-time

- probabilities of peak tornado wind speeds. *Wea. Forecasting*, **35**, 2479–2492, https://doi.org/10.1175/WAF-D-20-0010.1.
- Terrasson, A., N. McCarthy, A. Dowdy, H. Richter, H. McGowan, and A. Guyot, 2019: Weather radar insights into the turbulent dynamics of a wildfire-triggered supercell thunderstorm. *J. Geophys. Res. Atmos.*, **124**, 8645–8658, https://doi.org/10.1029/2018JD029986.
- Thurston, W., J. D. Kepert, K. J. Tory, and R. J. Fawcett, 2017: The contribution of turbulent plume dynamics to long-range spotting. *Int. J. Wildland Fire*, **26**, 317–330, https://doi.org/10.1071/WF16142.
- Tohidi, A., M. J. Gollner, and H. Xiao, 2018: Fire whirls. *Annu. Rev. Fluid Mech.*, **50**, 187–213, https://doi.org/10.1146/annurev-fluid-122316-045209.
- Tory, K. J., and J. D. Kepert, 2021: Pyrocumulonimbus firepower threshold: Assessing the atmospheric potential for pyroCb. *Wea. Forecasting*, **36**, 439–456, https://doi.org/10.1175/WAF-D-20-0027.1.
- ——, W. Thurston, and J. D. Kepert, 2018: Thermodynamics of pyrocumulus: A conceptual study. Mon. Wea. Rev., 146, 2579–2598, https://doi.org/10.1175/MWR-D-17-0377.1.
- Trentmann, J., and Coauthors, 2006: Modeling of biomass smoke injection into the lower stratosphere by a large forest fire (Part I): Reference simulation. Atmos. Chem. Phys., 6, 5247–5260, https://doi.org/10.5194/acp-6-5247-2006.
- Williams, A. P., J. T. Abatzoglou, A. Gershunov, J. Guzman-Morales, D. A. Bishop, J. K. Balch, and D. P. Lettenmaier, 2019: Observed impacts of anthropogenic climate change on wildfire in California. *Earth's Future*, 7, 892–910, https:// doi.org/10.1029/2019EF001210.
- Wu, J. M., A. D. Vakili, and F. M. Yu, 1988: Investigation of the interacting flow of nonsymmetric jets in crossflow. AIAA J., 26, 940–947, https://doi. org/10.2514/3.9994.
- Zhou, R., and Z. N. Wu, 2007: Fire whirls due to surrounding flame sources and the influence of the rotation speed on the flame height. *J. Fluid Mech.*, **583**, 313–345, https://doi.org/10.1017/S0022112007006337.